IN SITU TEM MICROPILLAR COMPRESSION TESTING IN IRRADIATED OXIDE DISPERSION STRENGTHENED ALLOYS

by

Kayla Haruko Yano

A thesis

submitted in partial fulfillment

of the requirements for the degree of

Master of Science in Materials Science and Engineering

Boise State University

August 2017

BOISE STATE UNIVERSITY GRADUATE COLLEGE

DEFENSE COMMITTEE AND FINAL READING APPROVALS

of the thesis submitted by

Kayla Haruko Yano

Thesis Title: *In Situ* TEM Micropillar Compression Testing in Irradiated Oxide Dispersion Strengthened Alloys

Date of Final Oral Examination: 24 April 2017

The following individuals read and discussed the thesis submitted by student Kayla Haruko Yano, and they evaluated her presentation and response to questions during the final oral examination. They found that the student passed the final oral examination.

Hui (Claire) Xiong, Ph.D.	Co-Chair, Supervisory Committee
Janelle Wharry, Ph.D.	Co-Chair, Supervisory Committee
Yaqiao Wu, Ph.D.	Member, Supervisory Committee
Brian Jaques, Ph.D.	Member, Supervisory Committee

The final reading approval of the thesis was granted by Hui (Claire) Xiong, Ph.D., and Janelle Wharry, Ph.D, Co-Chairs of the Supervisory Committee. The thesis was approved by the Graduate College.

DEDICATION

To my sisters, Treya and Aliya.

May we always keep pushing each other.

… even if it's just pushing each other over in an onion field.

ACKNOWLEDGEMENTS

To start, I would like to thank my advisor, Dr. Janelle Wharry, for her patience and endless support throughout this effort. Thank you especially to Dr. Claire Xiong for being willing to oversee my last year here at BSU and for the push to complete this thesis. I'd also like to acknowledge and thank my other committee members for their participation in this process.

Much of this work was conducted at the MaCS at CAES. Jatu Burns and Allyssa Bateman - thanks for sharing your wisdom and knowledge of the FIB. Joanna Taylor - thanks for accommodating my last-minute schedule changes. Dr. Yaqiao Wu - thank you for all your help on the TEM. Without your assistance loading my samples into the Picoindenter, I'm afraid many more samples would have been lost. Your expertise with the TEM was essential and saved me many grueling hours aligning the indenter tip.

Matthew Swenson - thanks for all your help in this endeavor. I appreciate all the time you took to teach me the ropes, all the long drives to Idaho Falls, and all the late-nights FIB-ing out samples. Your mentorship gave me a jump-start onto this whole graduate school process and I will always be grateful for your wise words and perspective.

This research was sponsored in part by the US Nuclear Regulatory Commission Grant NRC-HQ-84-14-G-0056, the Micron Foundation, and by the US DOE Office of Nuclear Energy under DOE Idaho Operations Office Contract DE-AC07-05ID14517, as part of the Nuclear Science User Facilities experiment 15-540.

ABSTRACT

The objective of this study is to determine the validity of *in situ* transmission electron microscopy (TEM) micro-compression of pillars in as received and ion-irradiated Fe-9%Cr oxide dispersion strengthened (ODS) alloy. The growing role of charged particle irradiation in the evaluation of nuclear reactor candidate materials requires the development of novel methods to assess mechanical properties in near-surface irradiation damage layers just a few micrometers thick. *In situ* TEM mechanical testing is one such promising method, yet size effects must be understood to validate the technique. In this work, a micro-compression pillar fabrication method is developed. Yield strengths measured directly from TEM *in situ* compression tests are within expected values, and are consistent with predictions based on the irradiated microstructure. Measured elastic modulus values, once adjusted for deformation and deflection in the base material, are also within the expected range. A pillar size effect is only observed in samples with minimum dimension ≤ 100 nm due to the low inter-obstacle spacing in the as received and irradiated material. By comparing the microstructural obstacle spacing with specimen dimensions, size effects can be understood and TEM *in situ* micropillar compression tests can be used to quantitatively determine mechanical properties of shallow ion-irradiated layers.

TABLE OF CONTENTS

LIST OF TABLES

LIST OF FIGURES

LIST OF ABBREVIATIONS

A	Area
a	Lattice Parameter
APT	Atom Probe Tomography
α_{CON}	Convergence Angle
α	Ferrite Phase of Iron
$\mathrm{\alpha}$	Strength of Obstacle Barrier
$\mathrm{\alpha}'$	Geometrical Constant for Dislocation Type
b	Burgers Vector
bcc	Body-Centered Cubic
bct	Body-Centered Tetragonal
BSU	Boise State University
β	Collection Angle
CAES	Center for Advanced Energy Studies
CCD	Charge Couple Device
D	Dislocation Size
d	Diameter of Tensile Sample
d	Characteristic Length
D_G	Guinier Diameter
$\mathrm{d_g}$	Grain Diameter

d_{max}	Max Diameter of Cluster
$\overline{d_{ob}}$	Weighted Average Diameter of Obstacles
dpa	Displacements Per Atom
Δl	Change in Length
$\Delta\sigma_y$	Increment in Yield Stress
$\Delta\sigma_{y,i}$	Increment in Yield Stress Due to *i* Obstacle Type
δ	Delta-Ferrite Phase of Iron
E	Elastic Modulus
E	Potential Energy Between Atoms
E_0	Equilibrium Potential Energy
E_A	Attractive Energy
E_R	Repulsive Energy
EELS	Electron Energy Loss Spectroscopy
ε	Strain
F	Force
FEM	Finite Element Model
FIB	Focused Ion Beam
fcc	Face-Centered Cubic
G	Shear Modulus
γ	Austenite Phase of Iron
i	Microstructural Obstacle Feature
IVAS	Integrated Visualization and Analysis Software
k	Material Constant Due to Dislocation Geometry and Type

L	Obstacle Spacing
L_{ob}	Average Obstacle Spacing
L_p	Length of Dislocation Pile-up
l_i	Instantaneous Length
l_0	Initial Length
λ	Angle Between Slip Direction and Loading Axis
M	Upper Limit of Uniaxial Yield Strength to Resolved Shear Strength Ratio
MEMS	Microelectromechanical System
N	Dislocation Number Density for *i* Obstacle
n	Number of Dislocations in Pile-up
$\mathrm{N_{min}}$	Minimum Number of Clusters
N_{nc}	Cluster Number Density
N_{ob}	Sum Number Density of All Obstacles
υ	Poisson’s Ratio
ODS	Oxide Dispersion Strengthened
PTP	Push-to-Pull
φ	Angle Between Slip Normal and Loading Axis
$\mathrm{R_g}$	Overall Radius of Gyration
$\mathrm{R_{gx}}$	Radius of Gyration in X-Direction
$\mathrm{R_{gy}}$	Radius of Gyration in Y-Direction
$\mathrm{R_{gz}}$	Radius of Gyration in Z-Direction
RIS	Radiation Induced Segregation

r	Atomic Separation
r_c	Dislocation Core Radius
r_o	Atomic Equilibrium Separation Distance
ρ	Dislocation Density
SEM	Scanning Electron Microscope
SRIM	Stopping and Range of Ions in Matter
SS	Stainless Steel
STEM	Scanning Transmission Electron Microscopy
ΣN_c	Total Number of Clusters Identified
ΣV_T	Total Analyzed Volume
σ	Engineering Stress
σ_0	Frictional Force Required to Move a Dislcoation
σ_y	Yield Strength
T_D	Line Tension Due to a Line Dislocation
TEM	Transmission Electron Microscopy
τ	Shear Stress
τ_a	Shear Stress Applied by a Dislocation Pile-up
τ_c	Critical Shear Stress to Pass Through a Grain Boundary
τ_{CRSS}	Critical Resolved Shear Stress
τ_0	Frictional Forces Required to Move Dislocation
τ_{Or}	Orowan Stress

CHAPTER ONE: INTRODUCTION AND MOTIVATION

Compared to current fission reactors, increased temperatures and irradiation damage doses will be reached in advanced fast fission reactors and fusion reactor designs. In the former, higher temperatures will improve thermal efficiency, but the higher neutron fluxes induce higher damage doses. In the latter, fusion reactions result in high doses. As such, there is an increasing need for advanced alloys in structural and cladding applications for both reactor types. These materials must withstand temperatures up to 700 ˚C and doses up to several hundred displacements per atom (dpa) [1–5]. ODS steels are of great interest for these applications due to their dimensional stability under irradiation and high temperature strength [6–23]. This work focuses on one such alloy, a model Fe-9%Cr ODS martensitic steel.

To evaluate the integrity of materials, including ODS steels, in reactor environments, they must undergo neutron irradiation testing. However, neutron irradiation testing of materials is time-consuming, costly, and causes radioactivation of samples. Charged particle irradiations are often used to emulate neutron damage, speeding up testing time by at least two orders of magnitude, with little to no radioactivity, and hence can be conducted at a fraction of the cost. However, ion irradiation does not necessarily provide a one-to-one comparison with neutron irradiation [22–30]. Differences in irradiating particle and temperature can cause vastly different microstructural damage, which can manifest as different mechanical properties [23]. However, ion irradiations remain attractive for their ability to quickly and cheaply test candidate alloys under a variety of conditions. Being able to attain meaningful mechanical properties from ion irradiated materials is of utmost importance in improving and validating models that allow us to then predict the behavior and performance of materials under high temperature and high neutron irradiation dose environments.

Another notable contrast between neutron and ion irradiations – and that which will be the motivation for this work – is the difference between their damage profiles. Figure 1.1 shows the damage profiles for neutrons, protons, and iron ion irradiation on a target material of Fe-9%Cr ODS as calculated using the Stopping and Range of Ions in Matter (SRIM) 2013 program in "Quick Calculation" (Kinchin-Pease) mode [31]. At 5 MeV, Fe^{2+} ion damage exhibits a steep gradient between the surface and the damage peak which is located approximately 1.2 µm from the surface. Damage from 2 MeV protons reaches further into the material, with a stable damage range between the surface and the peak, located at approximately 19 µm from the surface. Finally, neutrons create a uniform damage profile through the specimen.

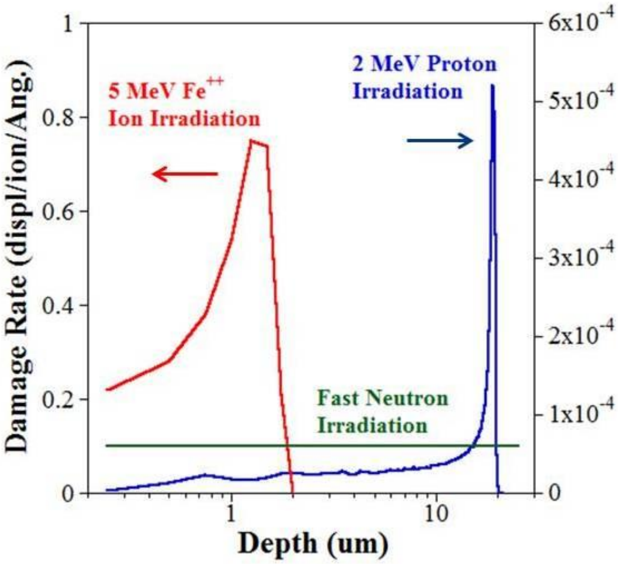

Figure 1.1 Damage profile as calculated by SRIM for Fe^{2+} ions, protons, and neutrons

Due to the shallow damage layer in both Fe^{2+} ion and proton irradiation, novel mechanical test methods to characterize candidate alloys must be developed to probe this shallow damage layer. Conventional scale tensile or compression specimens sample not only the shallow ion irradiated layer but also reach far into the bulk, unirradiated material. This can be seen in Figure 1.2a, in which the unirradiated bulk material dominates the mechanical response, rendering one unable to discern the influence of irradiation. However, the irradiated layer can be isolated, and the mechanical response can probe in just that layer, by reducing the tested specimen size. An example of this reduced specimen size is shown in Figure 1.2b, which is a microscale sample that can be focused ion beam (FIB) milled and mechanically tested *in situ* TEM. Overlayed on both is the damage profile (in orange). It is easily seen that conventional testing methods are unable to assess just the irradiation effects, whereas micromechanical testing methods only sample from the shallow ion irradiated layer.

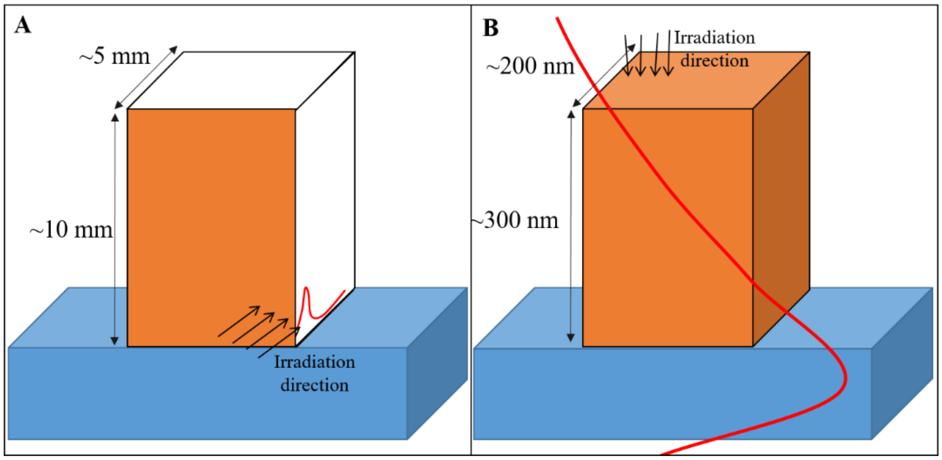

Figure 1.2 Example geometry and ion-irradiation damage profile overlay of (a) conventional vs. (b) *in situ* compression specimens

Yet, at the small length scales necessary for micromechanical testing, especially *in situ* TEM micromechanical testing, size effects are a concern. In pure metals, like copper [32–34], nickel [35,36], or single grained chromium [37] and magnesium [38], mechanical properties are inflated due to source truncation and exhaustion in the dimensionally constrained small specimen volumes. However, work on materials with more complex microstructures and even irradiated pure metals suggests that this size effect is less pronounced due to the reduced average spacing between obstacles, which serve as both sources and pinning points for dislocations [39–43].

We hypothesize that with reduced obstacle spacing, sample dimensions can be reduced to TEM scale. The objective of this work is to determine if *in situ* TEM micromechanical testing can be utilized to quantitatively determine yield stress and elastic modulus of a model Fe-9%Cr ODS alloy independent of size effects. In this thesis, Chapter 2 will provide an overview of the fundamentals of the examined ODS alloy and size effects. Then, a published peer-reviewed journal article that addresses the objective of this thesis will be presented in Chapter 3. Finally, conclusions and future work are presented in Chapter 4.

CHAPTER TWO: BACKGROUND

The objective of this chapter is to give the reader a detailed understanding of the size effects in TEM *in situ* testing. This will be a four-step process, starting with the basics and moving into more refined understandings, specific to the material used in this study, Fe-9%Cr ODS, and specific to the micro-compression technique used.

The process begins with a fundamental understanding of mechanical responses in metals. This includes elastic deformation, dislocation motion and plastic deformation, strengthening mechanisms, and the stress-strain relationship.

With the knowledge of mechanical responses in general metals, we'll then step into the specifics of Fe-9%Cr ODS behavior. The major microstructurally-based strengthening mechanisms employed in this alloy will be discussed. Then the changes to this microstructure, and hence to mechanical properties, due to ion irradiations will be explained.

Next, a comparison of conventional vs. micro-mechanical testing methods will be provided. This will highlight the major techniques used in both size regimes: tensile, compression, and indentation/hardness testing. A more detailed look at micro-compression testing will be undertaken.

Finally, there will be a discussion on the methods required to resolve and understand the size effect issues seen during general *in situ* TEM micro-compression testing and testing of Fe-9%Cr ODS.

2.1 Fundamentals of Mechanical Responses in Metals

2.1.1 Bond Stretching and Elastic Deformation

In a solid, atoms are bonded to each other at an equilibrium separation distance, r_o, that minimizes the energy, E_0. In Figure 2.1, the potential energy, $\mathbf{E}$, is shown as a function of atomic separation, r. It is the sum of repulsive, E_R, and attractive, E_A, energies between atoms.

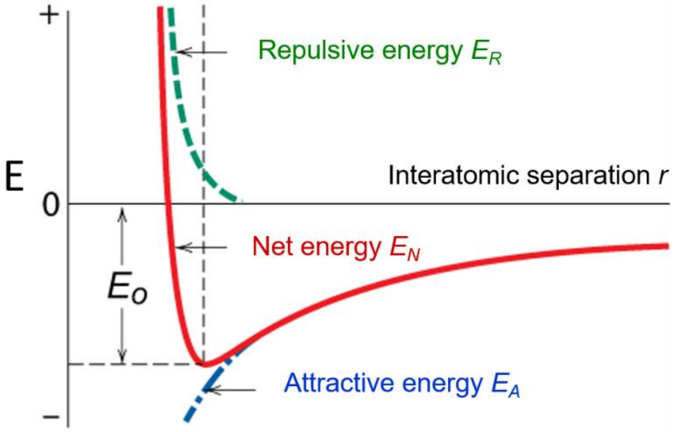

Figure 2.1 Energy-separation profile – adapted from [44]

By taking the derivative of the energy with respect to the separation distance, the force, F, between the atoms can be found. Figure 2.2 shows this relationship.

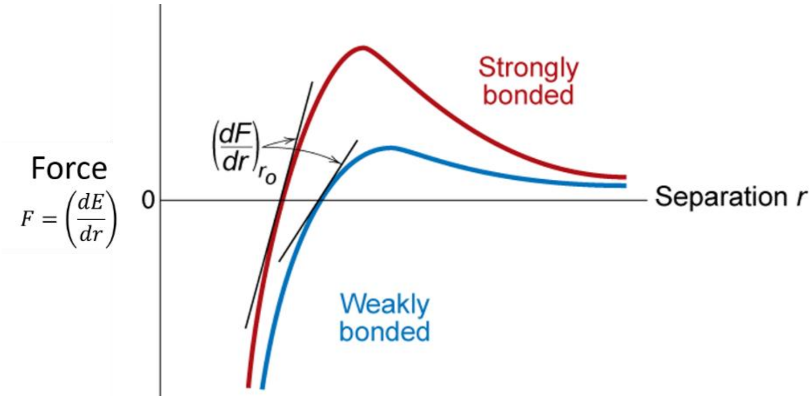

Figure 2.2 Force-separation profile – adapted from [44]

A nonpermanent deformation, or elastic deformation in a material is simply a stretching (or compression) of the equilibrium bond length between atoms. The elastic modulus, *E*, is a measure of the resistance to stretching of those bonds, given in Figure 2.2 as the derivative of the force with respect to the separation at the equilibrium separation distance. As can be seen, a strongly bonded, high elastic modulus, material has a larger slope than a weakly bonded, low elastic modulus material. As such, there is more resistance to the stretching of the atomic bonds in high modulus materials.

2.1.2 Dislocation Motion and Plastic Deformation

In a crystalline material there are two main types of dislocations, edge and screw. The edge dislocation arises from an incomplete plane of lattice atoms (sometimes called a half-plane); the edge of this incomplete plane forms the dislocation line. Compression is felt by the atoms above the dislocation line, whereas tension is felt by the atoms below the dislocation line. A screw dislocation occurs when there is a shear in the material, causing some of the atomic planes to slip or shift with respect to the remaining planes. Often a dislocation will be mixed, with both screw and edge characteristics. The various types of dislocations can be seen in Figure 2.3.

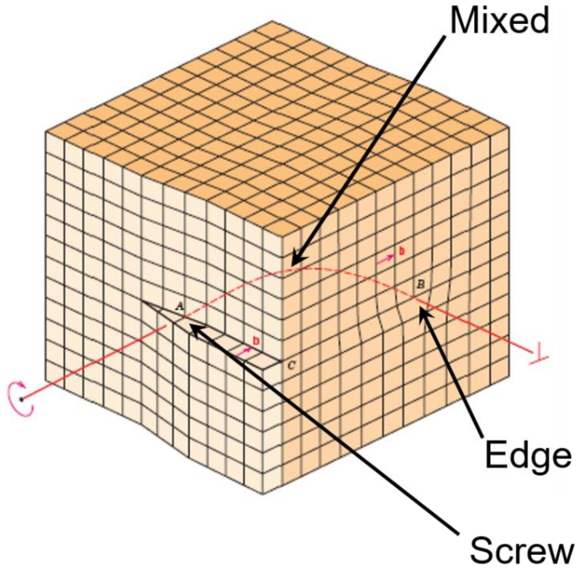

Figure 2.3 (a) Edge, screw, and mixed dislocation – adapted from [44]

The Burgers vector, *b*, gives the magnitude and direction of the dislocation from what would otherwise be a perfect crystal lattice. In edge dislocations the Burgers vector is perpendicular to the line dislocation and in screws they are parallel. As can be seen in the figure above, the Burgers vector stays the same throughout the mixed dislocation.

Plastic deformation in materials, or permanent deformation, occurs when a load applied to the material begins to move these dislocations through the material. Here the atomic bonds are breaking then re-forming with different atoms, not merely stretching as in elastic deformation. The point at which plastic deformation begins is given by the material property, σ_y, yield strength. Section 2.1.4 will discuss how this value is measured. The important thing for now is understanding how a dislocation can move.

Figure 2.4, adapted from [44], demonstrates the simple movement of an edge dislocation under shear. The extra half plane of atoms, plane A in Figure 2.4a, consecutively breaks and moves an interatomic distance until it reaches the surface of the crystal lattice at plane D.

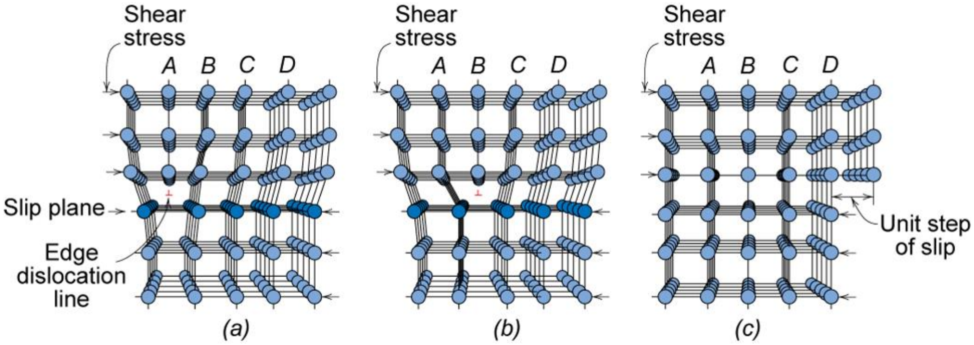

Figure 2.4 (a) Edge dislocation motion under shear load – adapted from [44]

This plastic deformation produced by dislocation motion is called slip. And the plane that the slip occurs is indicated in Figure 2.4 as well. This slip plane is the preferred plane for dislocations to move along; this direction is called the slip direction. The combination of slip plane and direction results in the slip system. For body-centered cubic (bcc) iron there are a few slip plane families {110}, {211}, {321} that result in a single slip direction $\langle 111\rangle$. This gives a Burger's vector of $b = \frac{a}{2}\langle 111\rangle$, where a is the lattice parameter [44].

In a single crystal, deformation occurs along these slip planes in the material. The load needed to start the slip motion is called the critical resolved shear stress which can be related to the yield stress through the following equation, where the angles φ and λ are measured between the slip normal and slip direction, respectively, to the loading axis.

$$\sigma_y = \frac{\tau_{CRSS}}{(\cos\varphi\cos\lambda)_{max}}$$ **Equation 2.1** [45]

These planes and angles can be seen in Figure 2.5a. 2.5b shows idealized macroscopic slip events in a single crystal.

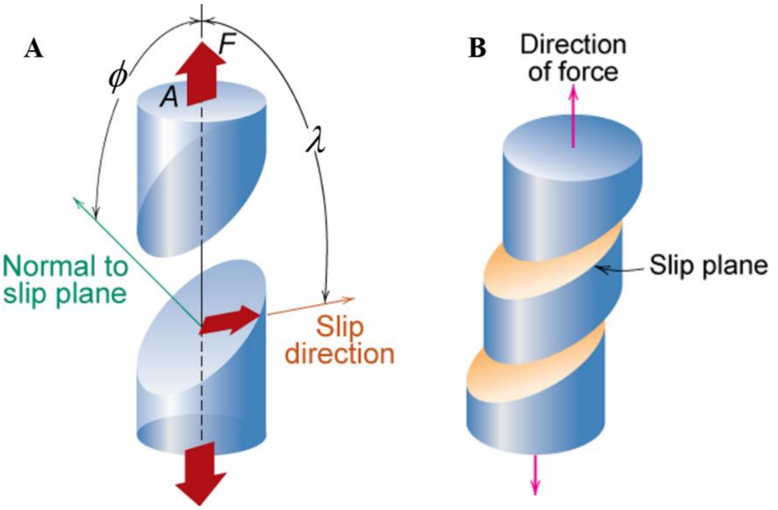

Figure 2.5 (a) Slip and normal planes to uniaxial tensile load (b) idealized macroscopic slip events in a single crystal – adapted from [44]

In polycrystalline materials, dislocations will move the same way they do in single crystals, however there are grain boundaries that can hinder dislocation motion. Some grain boundaries will be more or less favorably oriented to permit dislocations to transmit through them [44]. This increases the strength of the material. This strengthening mechanism, as well as a few other mechanisms, will be discussed in the following section.

2.1.3 Strengthening Mechanisms

Now that there is a basic understanding of dislocations and their motion, we can discuss the various methods used to slow dislocation movement in steels. By retarding the dislocation motion we can increase the yield strength. There are three basic strengthening mechanisms: 1) solid solution hardening, 2) dispersion or precipitate strengthening, and 3) grain size refinement.

While discussing these strengthening mechanisms, keep in mind that there are two constraints on a material when it comes to size effects. First, is the set of microstructural constraints, which is defined by the microstructure of the material. The other is the dimensional constraints, which is determined by the specimen size; specimen sizes can generally be classified as either bulk samples (dimensions in the m-mm range) or micro-mechanical (dimensions in the nm-μm range). Size effects occur when these two sets of constraints, microstructural and dimensional, reach the same scales. The fundamentals of mechanical responses begin to change. It is essential to understand the microstructure in context of the dimensions of the tested specimens to validly utilize micro-mechanical testing. The three strengthening mechanisms discussed here all affect the microstructural constraints.

Further, there are two sub-categories of microstructural constraints in metals. The first is the characteristic length; one of the most fundamental of types being a Burgers vector of a dislocation. The Burgers vector gives the magnitude and direction of the dislocation. It is a measure of the strength of the lattice distortion caused by the dislocation's presence; it *characterizes* the strength of the lattice distortion [45]. The second sub-category is the size parameter; this could be grain size or obstacle spacing [45]. The interaction of the two, characteristic length and size parameter, has a direct relationship to the microstructural constraint on yield strength. Where applicable, these labels will be used in the following discussion of each strengthening mechanism.

In solid solution hardening, impurity atoms introduce lattice strains on the surrounding host atoms: compressive for larger impurities, tension for smaller impurities. This compressive effect can be seen in Figure 2.6a for a larger impurity atom. Figure 2.6b shows how impurity atoms tend to congregate around dislocations to reduce the lattice strain introduced by the dislocation. This strengthens the alloy because any slip would need to move those impurity atoms and the lattice strain would increase [44]. Here the microstructural constraint is defined by the interaction of the edge dislocation (characteristic length) and the impurity atom (size parameter).

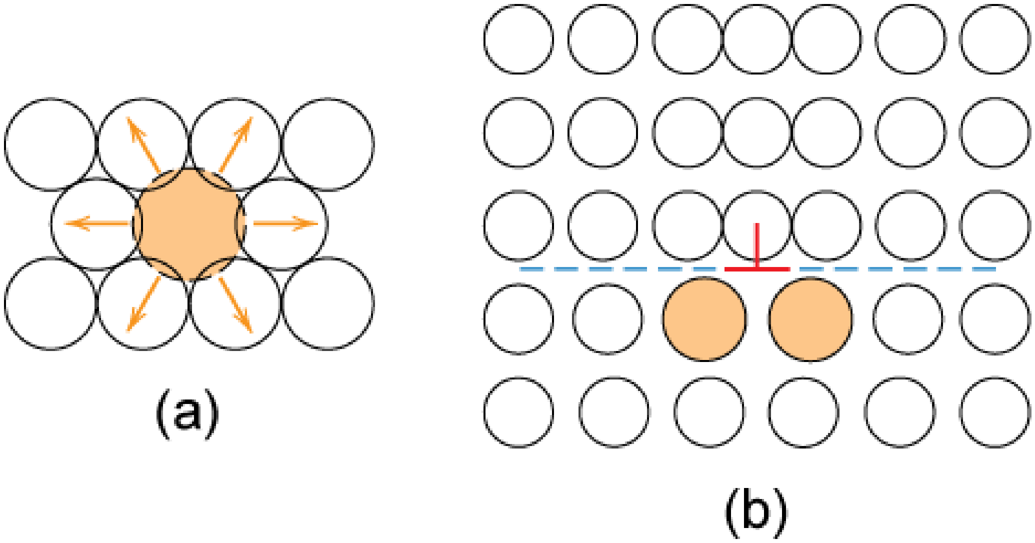

Figure 2.6 Effect of impurity atoms in a lattice – adapted from [44]

Precipitation/dispersion strengthening occurs when small phases or particles, respectively, act as barriers to dislocation motion [19,22,44,46,47]. As a line dislocation attempts to move past a particle, it has an inherent line tension that resists bending around the particle. This is given by:

$$T_d = \frac{Gb^2}{2}$$ **Equation 2.2** [45]

where G is the shear modulus. The characteristic length is the diameter of a curved dislocation (or loop), d, under a shear stress, τ. This diameter is given by:

$$d(\tau) = \frac{Gb}{\tau}$$ **Equation 2.3** [45]

Now that we have the characteristic length, we must try and understand how it interacts with the various particle types or size parameters found in advanced alloys.

The most straightforward is the Orowan mechanism. Here the dislocation must fully bypass the obstacles to result in plastic deformation. As can be seen in Figure 2.7, the size parameter of note is the obstacle spacing, *L*. As the characteristic length, *d*, approaches the obstacle spacing (2.7b), the dislocation can move past the obstacles.

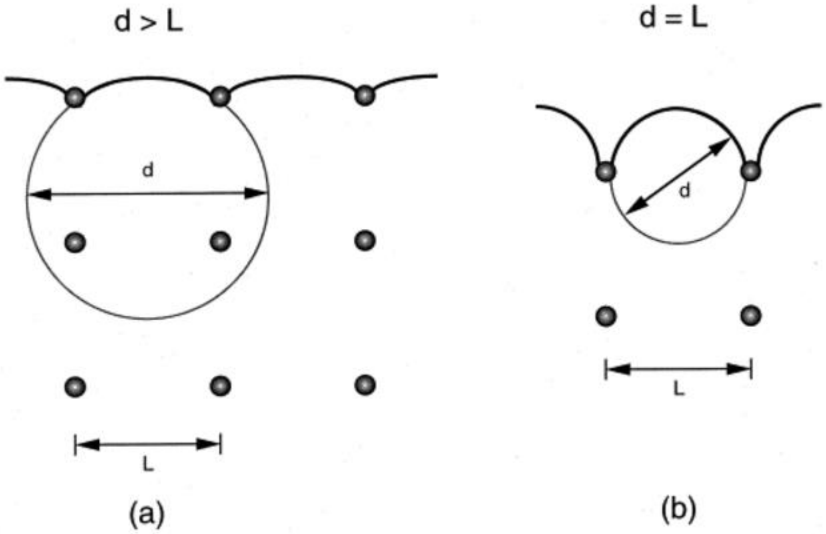

Figure 2.7 Orowan mechanism relating the characteristic length, *d*, with the obstacle spacing, *L* – reproduced from [45]

We can then adjust Equation 2.3 using the Orowan stress, τ_{Or}, and the obstacle spacing.

$$\tau_{Or} = \frac{Gb}{L}$$ **Equation 2.4** [45]

As the dispersion of particles becomes more even throughout the alloy and there results a 'dislocation forest,' the average obstacle spacing, L_{ob}, can be taken on average and related to the dislocation density, ρ, through:

$$L_{ob} = \frac{1}{\sqrt{N_{ob}\overline{\overline{d_{ob}}}}.}$$ **Equation 2.5** [45]

Where the dislocation density is the product of the sum number density of all obstacles, N_{ob}, and the weighted average diameter of the obstacles, $\overline{d_{ob}}$. Then substituting Equation 2.5 into 2.4 results in the classical work-hardening Taylor equation:

$$\tau = \alpha G b \sqrt{N_{ob}\overline{d_{ob}}}$$ **Equation 2.6** [45]

Where α is a factor describing the penetrability of the obstacles. In steels, α can be found through the following relationship:

$$\alpha = \frac{1}{2\pi}\ln\left(\frac{l}{2r_c}\right)$$ **Equation 2.7** [48]

Where r_c is the dislocation core radius. Listed are some general values for α of different obstacle types. In precipitates and voids that cause bowing α=1, and for cutting α=0.3-0.5. For dislocation loops α=0.25-0.5 and for black dots α<0.2, but α values can also vary with the size of these obstacles [48].

Grain size refinement is the last strengthening mechanism to be discussed. The number and size of the grains is extremely important to dislocation motion. Grain boundaries act as additional obstacles (size parameters) for the dislocations (characteristic lengths) to interact with. The more incoherent the boundary, the more energy it takes to move a dislocation across it. Hence the material is strengthened with an increase in grain quantity, or reduction in grain size.

This increase in energy comes from dislocations in a material that will build up, or pile-up, along grain boundaries. The resolved shear stress on the slip plane applied by a dislocation is, τ_a, and therefore the stress at the head of the pile-up is $n\tau_a$, where n is the number of dislocations in the pile-up. The number of dislocations in a pile-up is related to the length of the pile-up, L_p, and that is proportional to the grain diameter through:

$$L_p = \frac{\alpha' \mathrm{nGb}}{\pi \tau_a}$$ **Equation 2.11** [49]

Where α' is a geometrical constant equal to 1 for screw dislocations and (1-υ) for edge dislocations. υ is Poisson's ratio. If the source of the pileup is located at the center of the grain, then $L_p = d_g/2$, where d_g is the grain diameter. If the stress required to pass through the grain boundary is τ_c, then:

$$\tau_c \leq \frac{\alpha' \pi d_g \tau_a^2}{2Gb}$$ **Equation 2.12** [49]

The friction forces required to move a dislocation without obstacles is τ_0 so that we end up with the Hall-Petch relationship:

$$\tau_a \geq \tau_0 + k d_g^{-\frac{1}{2}}$$ **Equation 2.13** [49]

Equation 2.13 can also be modified for yield strength as shown below:

$$\sigma_y = \sigma_0 + k d_g^{-\frac{1}{2}}$$ **Equation 2.14** [44]

Where σ_0 and k are constants of the material due to frictional forces required to move a dislocation and the geometry of the dislocations, respectively. Additionally a reduced grain size not only improves strength, it also increases the toughness of alloys [44]. Grain size refinement uses the interaction between characteristic length (dislocation pile-up) and size parameters (grain size) to improve mechanical properties of the alloy.

The Hall-Petch equation's accuracy varies with the alloy system and the grain size range [49]. As can be seen in Figure 2.8 below, the grain size range at which the Hall-Petch relationship is most accurate is between 10-100 µm. For smaller grain sizes, <10 µm, the yield stress is limited by the maximum theoretical strength because of the availability of a dislocation source. In the normal Hall-Petch grain size range, the yield stress is that required to move the already existing dislocations. But at the smaller grain sizes – and this also holds for smaller specimen dimensions – fewer dislocations are available within each grain, and their population is insufficient to induce plasticity. Thus, the stress required is that needed to create dislocations that will subsequently move through the material during plastic deformation [45].

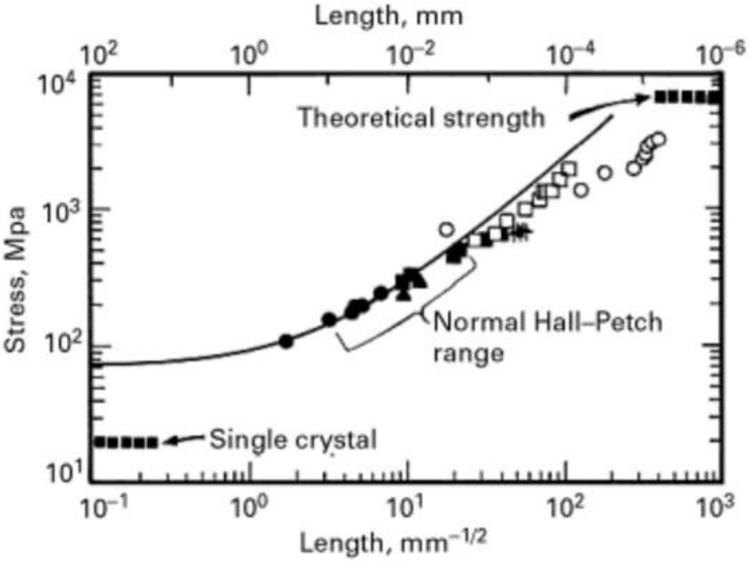

Figure 2.8 Hall-Petch plot for iron and low-carbon steel across grain sizes ranging from 100 µm to 1 nm – adapted from [49]

Each type of obstacle (precipitates, voids, dislocation loops, black dots, or grain boundaries) add to the yield stress increment, and modifying Equation 2.6 results in the yield stress increment, $\Delta\sigma_y$, instead of the shear stress, τ, for any type of obstacle.

$$\Delta\sigma_y = \alpha M G b \sqrt{ND}$$ **Equation 2.8** [48]

Where *N* is the dislocation number density, *D* is the dislocation size (obstacle size parameter), and *M* is an upper limit for the ratio of uniaxial yield strength to resolved shear strength. *M* is 3.06 for bcc lattices [48].

Altogether the total yield stress increment due to the dispersed obstacles in the microstructure is generally a linear superposition for obstacles with dissimilar strengths shown below:

$$\Delta\sigma_y = \sum_i \Delta\sigma_{y,i}$$

Equation 2.9 [48]

Or a root-sum-square superposition for obstacles with similar strength.

$$\Delta\sigma_y = \sqrt{\left(\sum_i \Delta\sigma_{y,i}\right)^2}$$

Equation 2.10 [48]

Where the subscript *i* denotes each type of obstacle. Again, Equation 2.10 ultimately describes the relationship between a characteristic length (of the dislocation forest) and the size parameter (of the obstacles inhibiting the dislocation motion).

2.1.4 Mechanical Properties – Yield Strength and Elastic Modulus

In Section 2.1.1 we learned that elastic deformation comes from atomic bond stretching and that the elastic modulus is a measure of this bond energy. Section 2.1.2 explains how plastic deformation comes from dislocation motion and that the accepted measure of the onset of plastic deformation is the yield strength, σ_y. The various strengthening mechanisms within the microstructure that inhibit dislocation motion and improve yield strength were discussed in Section 2.1.3.

Now that yield strength and elastic modulus have been conceptually defined, the actual method of calculating both will be discussed. This section will look at the equations used to find both in mechanical testing.

To understand yield strength and elastic modulus, an understanding of stress and strain must first occur. Engineering stress, σ, is the force, F, exerted along the initial cross-sectional area, A, as shown in Equation 2.15.

$$\sigma = \frac{F}{A}$$ **Equation 2.15**

Engineering strain, ε, is measured as the change in length, Δl, over the initial length, l_0, and where l_i is the instantaneous length.

$$\varepsilon = \frac{l_i - l_0}{l_0} = \frac{\Delta l}{l_0}$$ **Equation 2.16**

Stress and strain are related through the elastic modulus, E, in the elastic region of deformation in a material through Hooke's Law.

$$\sigma = E\varepsilon$$ **Equation 2.17**

This region is linear under both load and unload and often only applies to small strains in the material, especially in steels [44].

Yield strength, σ_y, signifies the onset of plastic deformation and is often measured using the 0.002 strain offset method. This is shown in Figure 2.9. At 0.002 strain, a line with slope given by the load curve, E, intersects the stress-strain curve resulting in the yield stress, σ_y, or the point at which elastic deformation turns to plastic deformation.

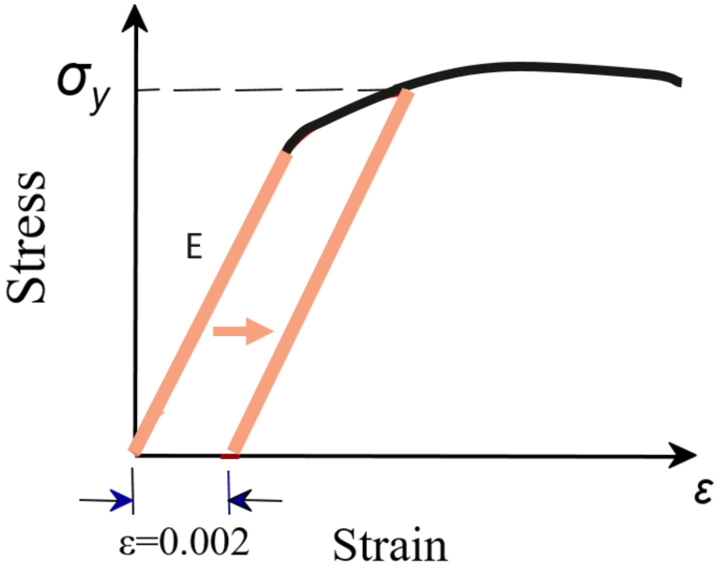

Figure 2.9 Stress-strain curve showing yield strength measurement through 0.002 strain offset – adapted from [44]

2.2 Understanding of ODS Behavior

Now that there is a basic understanding of the fundamentals of mechanical responses of metals due to dislocations and strengthening mechanisms in the microstructure we can take a specific look at the material studied in this work, Fe-9%Cr ODS. This will begin by looking at the unirradiated microstructure and accompanying mechanical properties, then work into the changes induced by ion irradiation.

Iron-chromium (9-12 wt%) ferritic/martensitic steels have long been used in power-generation as boiler and turbine materials. The 1970’s, however, was the first time this set of steels was considered for cladding and structural materials in nuclear reactors. Work on this set of materials is being conducted by all the major geographical nuclear powers: Japan, the European Union countries, and the United States [50].

These materials are attractive for nuclear applications because of their high-temperature strength and dimensional stability under irradiation. An additional advantage is reduced or low-activation found in these materials. As reactors are maintained and upgraded, waste or left-over structural materials must be disposed of or recycled and a reduced activation is key to the safe disposal of these materials [50].

A great deal of work has been done on this class of materials to understand its performance with different alloying elements, different processing methods, and under different particles and levels of irradiation. In this thesis, only a model Fe-9%Cr steel is used and as such, only prior work on this material will be discussed. For detailed understandings of other compositions of Fe-Cr alloys see ref. [50].

Through these various hardening mechanisms, Fe-9%Cr has been tailored to perform with minimal microstructural change within fast fission and fusion environments. The uniform oxide dispersion, small grain size, and high dislocation density make it ideal for a high temperature and high dose environment. In Section 2.2.2 the influence of irradiation on the as received microstructure will be discussed. Section 2.3.1 will provide the yield strength and modulus results from bulk testing of the as received and irradiated material.

2.2.1 As-Received ODS

Nuclear-relevant ODS alloys are often based on an Fe-Cr alloy matrix, which takes a ferrite, martensite, or a duplex ferritic-martensitic (F-M) structure. To produce martensite, austenite (γ iron) must be quenched rapidly such that diffusion does not occur. The atoms in the austenite face-centered cubic (fcc) structure quickly shift to body-centered tetragonal (bct) positions. This is a non-equilibrium condition and carbon atoms sit in interstitial locations [44]. Martensite is often tempered below 650˚C to relax internal stresses formed during the transition from fcc to bct. Under these conditions, the resulting microstructure is a mix of residual fine ferrite (α) grains and austenite (γ) converted martensite phase [47,51].

The alloying elements, C, N, Ni, and Mn extend the γ-phase field, while the elements Cr, W, Si, and Ti contract it [50]. The latter elements also form more δ-ferrite. C is the cheapest austenite former, but reduces the toughness of the alloy and results in coarser grain sizes [50]. A balance must be made between the two groups of alloying elements and their accompanying resultant phases.

In this Fe-9%Cr ODS, the matrix element is iron (Fe). It is mechanically alloyed with other elements, chromium (Cr), carbon (C), tungsten (W), titanium (Ti), yttrium oxide (Y_2O_3), iron-yttrium intermetallic compound (Fe_2Y), and iron oxide (Fe_2O_3) powders through ball milling for 48h in an argon gas atmosphere. The resulting powder is sealed in cans and degassed at 673K in a vacuum of 0.1 Pa. This was then hot-extruded at 1423 K and air-cooled [47]. The detailed composition of this model Fe-9%Cr ODS alloy is listed in Table 2.1.

Table 2.1 Chemical composition of model Fe-9%Cr ODS alloy

Chemical Composition (wt.%, balance Fe)														
C	Si	Mn	P	S	Ni	Cr	W	Ti	Y	O	N	Ar	Y_2O_3	Ex. O
0.14	0.048	0.05	<0.005	0.004	0.06	8.67	1.96	0.23	0.27	0.14	0.017	0.004	0.34	0.07
$[Y_2O_3] = 1.27 \times [Y]$														
[Ex.O] = [Total O] – [O in Y_2O_3 powder] = [O] – 0.27 x [Y]														

This results in a fully martensitic Fe-Cr alloy. The calculated phase diagram for this alloy is shown in Figure 2.10, reproduced from [47].

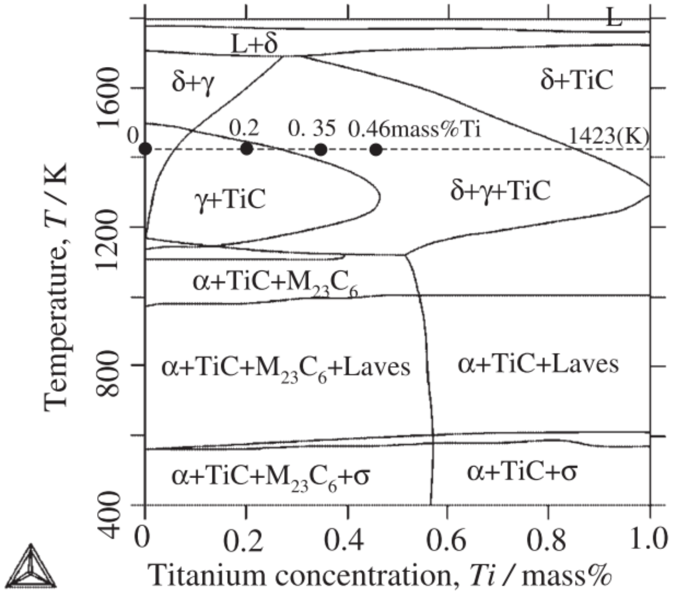

Figure 2.10 Fe-9%Cr phase diagram predicting a fully martensitic alloy – reproduced from [47]

By adding in elements above their solution limits and uniformly dispersing the Y_2O_3 oxides within the matrix, dislocation motion is retarded and the material is strengthened. The Y_2O_3 oxides provide high-temperature stability of the alloy because it exhibits little to no dissolution or growth under increased temperature [19,52,53].

As we know from section 2.1.3 any obstacle to dislocation motion, including precipitates, grains, dislocation lines, dislocation loops, voids, and oxide nanoclusters, can contribute to the strength of a material. Efforts have been made to quantify the density of these obstacles and calculate their resultant impact on yield strength for the exact material being used in this work [54]. A summary of the data will be provided in Chapter 3.

Using TEM, approximately 100 grains and 36 carbide precipitates were measured. The effective grain diameter is 0.23 μm. Carbide precipitate effective diameter was 0.11 μm with a density of 0.20×10^{20} m^{-3}. The density of dislocation lines was measured to be

19.1×10^{14} m^{-2}. Using atom probe tomography (APT) analysis, 486 oxide nanoclusters were measured in an analysis volume of 856,053 nm^3 resulting in a density of 568×10^{21} m^{-3} [54]. From these measurements, an average obstacle spacing can be calculated using Equation 2.5. For the as received material $L_{ob} = 17.2$ nm.

A TEM micrograph of the as received material is shown in Figure 2.11. Notice the variety of microstructure adding to the strength and toughness of the alloy: oxide nanoparticles (black small dots), grain boundaries, and dense dislocation regions.

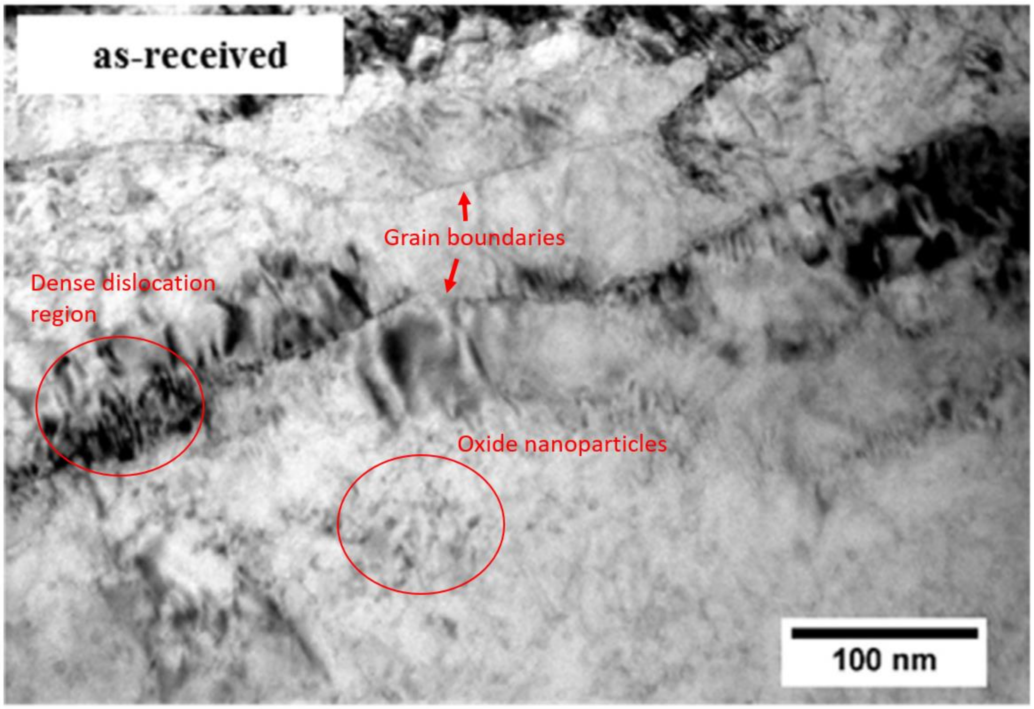

Figure 2.11 TEM micrographs of as received Fe-9%Cr – adapted from [23]

2.2.2 Irradiated ODS

Irradiation introduces a variety of changes in a material. As energetic incident particles collide with atoms in the lattice, damage cascades propagate. These regions consist of interstitial and vacancy defect clusters, often Frenkel pairs, that can cluster and recombine to induce phenomena including: radiation induced segregation (RIS), irradiation induced precipitates, dislocation loops, and voids [48]. Whether these phenomena occur, and the extent to which they occur, depends on irradiating particle, irradiation dose, temperature, and the original microstructure of the material being irradiated [22,23,48,51].

Irradiation induced precipitates, loops, and voids act in the same way as the hardening mechanisms discussed above: they provide obstacles to dislocation motion. We can measure the number, density, and diameter of each of these using the same TEM technique as used for the as received material. The Fe-9%Cr was irradiated under two different Fe^{2+} conditions. The first was to a dose of 3 dpa at 500°C and the second was to 100 dpa at 500°C.

For the 3 dpa 500°C irradiation, 104 grains were measured with an effective diameter of 0.28 μm. 48 carbides were measured with an effective diameter of 0.08 μm a density of 0.76×10^{20} m^{-3}. Dislocation line density was 22.6×10^{14} m^{-2}. 48 dislocation loops were measured with a density of 2.1×10^{21} m^{-3}. No voids were seen. Oxide nanocluster density was measured to be 171×10^{21} m^{-3}. This resulted in an average obstacle spacing of 33.7 nm. For the 100 dpa 500°C irradiation, 105 grains were measured with a larger effective diameter at 0.37 μm. Carbide density went down to 0.29×10^{20} m^{-3}. Dislocation line density reduced at 18.4×10^{14} m^{-2}, while dislocation loop density increased to 4.3×10^{21} m^{-3}. Nanocluster density was near as received density at 513×10^{21} m^{-3}. The average obstacle spacing was calculated to be 18.9 nm. More details about the irradiation experiments and the irradiated microstructures will be provided in Chapter 3.

In this Fe-9%Cr ODS, the root-sum square approach has been shown to be more accurate in calculating the incremental strength contribution from each obstacle type [22]. The barrier strength, α, for each obstacle type can be calculated using Equation 2.7. Then using Equation 2.10 the microstructurally predicted strength change can be calculated for each irradiation condition. In the 3 dpa condition $\Delta\sigma_y$ = 15 MPa and in the 100 dpa condition $\Delta\sigma_y$ = 43 MPa. Both predicted values suggest that any strengthening added by the irradiation-induced nucleation of dislocation loops is offset by the softening from the decrease in size and number density of oxide nanoclusters at 500°C.

2.3 Mechanical Testing

As discussed in the prior section, the dispersed barrier strengthening model can be used to predict strength changes in irradiated materials from the microstructure as measured by TEM and APT. However mechanical tests are still needed to confirm microstructural predictions. Traditionally these tests have been conducted on bulk materials, yet due to the near-surface damage layer found in ion irradiated materials, many different *in situ* micro-mechanical test methods have been developed.

Conventional bulk tests consist of tensile, compression, hardness, Charpy fracture, bending, etc. All of these are conducted on samples in the millimeter or larger scale range. *In situ* testing consists of similar methods – e.g. tensile, compression, nanoindentation, micro-beam fracture – but can range in size from micrometer to nanometer. Generally, the micrometer scale samples are tested *in situ* scanning electron microscope (SEM). However, when testing irradiated samples using *in situ* SEM approaches, it can still remain difficult to separate the influence of the unirradiated substrate from the mechanical performance measured due to the shallow damage layer (Figure 1.1).

Conventional bulk testing and *in situ* micro-mechanical testing methods differ in scale but are often analogous in process. Bulk and micro-scale materials testing each utilize uniaxial tensile and compression tests; bulk hardness testing is similar in idea to nanoindentation testing. In the following section a description of these more prevalently used methods in both conventional and micro-mechanical testing is provided; their application to irradiated alloys, and specifically to ODS alloys if available, are also described.

2.3.1 Conventional Mechanical Testing

Uniaxial tensile and compression testing are amongst the most straightforward mechanical test methods. In tensile testing a dog-bone shaped sample is prepared (mm-scale) and installed in a tensile tester. The cross-section of the sample can be circular or rectangular, but by using a reduced cross-section, the eventual plastic deformation can be constrained to the gauge length. An example of a tensile sample is shown in Figure 2.12. The load is measured with a load cell and the elongation can be measured with an extensometer.

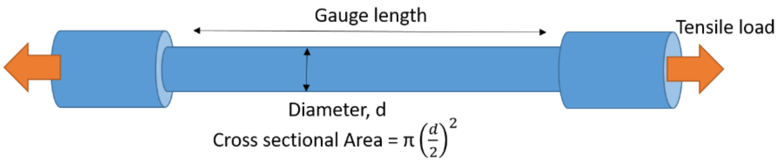

Figure 2.12 Tensile sample with cross-sectional area defined

Knowing the load, displacement, initial cross-sectional area and length, the engineering stress and strain can be calculated using Equations 2.15 and 2.16 from

Section 2.1.4. Figure 2.13 shows the general shape of a tensile specimen tested to fracture for a bcc steel.

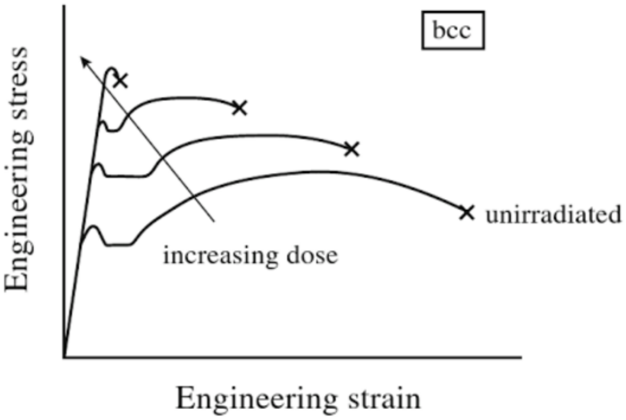

Figure 2.13 General behavior of ferritic (bcc) steel – adapted from [48]

Additionally, Figure 2.13 shows the general behavior of irradiated steels with increasing dose. Irradiation phenomena enhance the hardening effects to a point where the material loses its desirable attributes; it becomes too brittle to use safely. As such, an ideal material to be used in high dose environments is one that can 'absorb' the irradiation induced phenomena into its existing microstructure.

Compression testing is similar to tensile testing in that the load is uniaxial. However, failure is not as obvious to measure as samples do not cleanly fracture in compression. Yet, the calculation for stress and strain are identical and the calculation of yield strength and elastic modulus are readily accessed.

Hardness testing is the measure of a material's local resistance to plastic deformation. Hardness testing is simple, inexpensive, and nondestructive and is therefore used more frequently than other test methods [44]. Because the hardness test is a comparison between known material's hardness there are multiple scales that can be used. These include, Rockwell, Vickers, Knoop, and Brinell hardness testing, each with their own indentation tip material and shape. For well-studied materials hardness values can be converted to yield strength and elastic modulus values using empirical data [44].

Bulk mechanical property testing on Fe-Cr alloys have been conducted in the literature in both the as received [11,46,47,55–59] and irradiated [60–62] conditions. In general, the response of an irradiated Fe-9%Cr alloy is to increase both the yield strength and ultimate tensile strength, while reducing ductility as shown in the figure above.

Tensile testing has been conducted on a variety of different Fe-Cr alloys. Toualbi found yield strengths between 1000 and 1200 MPa for an Fe-9%Cr-1%W-0.2%Ti-0.3%Y_2O_3 alloy [59]. Two Fe-14%Cr alloys tested by Fournier resulted in yield strengths of ~1100 MPa [58]. Using an Fe-9%Cr with varying Y_2O_3 wt.%, Shi found a range of yield strengths between 1000-1200 MPa at room temperature [57]. Ohtsuka, using the same Fe-9%Cr-0.2%Ti as in this study, found a yield strength of ~300 MPa [47].

Tensile tests on irradiated alloys show an increase in yield strength. Lucon tested an Fe-9%Cr-1%W-0.2%V-0.1%Ta alloy and found an increase in yield strength of ~400 MPa after irradiating with neutrons to 1.73 dpa [62]. Henry tested a variety of Fe-Cr alloys all showing an increase in yield strength with irradiation dose [61].

Ohtsuka [47], Miyata [56], and Toualbi [59] all used a Vickers hardness testing method for their respective unirradiated Fe-Cr alloys. Toualbi found Vickers hardness values between 300-400 Hv. Miyata, varying the ferrite wt.%, found a range of 4.2-5 GPa. Ohtuska found a range of Vickers hardness values of 340-370Hv.

Zinkle collected literature data on Fe-8%Cr and Fe-9%Cr finding a range of elastic moduli of 192-216 GPa between room temperature and 450˚C [60]. Toualbi's measurements resulted in a range of between 190-220 GPa [59].

As can be seen, some of the most prevalent conventional tests in the literature are hardness and tensile testing. This is due to their relative ease of use to perform on a variety of shapes and sizes of bulk material. The techniques discussed in the next two sections can further expand the valuable range of material tested by reducing the amount of material required- a reduced activation volume for neutron irradiations or probing of only the ion-irradiated layers.

2.3.2 Nanoindentation and Micro-Tensile Testing

Nanoindentation and micro-tensile testing are amongst the most common miniature mechanical testing methods for both TEM and SEM *in situ* approaches. Nanoindentation is a relatively simple test to conduct, but much more complicated than uniaxial tests when it comes to analyzing the results. To start, the sample is polished and placed into a nanoindenter. Two indenter tips are generally used: Berkovich and spherical [22,42,63–66]. Berkovich tips directly result in hardness values and elastic modulus (which can be found during the unload curve of the indent). Yield stress can be related to the hardness measurements, but it is important to note that this relationship is empirical in nature. Spherical tips allow for a more direct analysis of yield strength as shown in ref. [67].

Nanoindentation testing of ion irradiated materials is typically done in one of two possible configurations. The first is “top-down” indentation on the irradiated surface, with indent directions parallel to the irradiation direction. This requires an understanding of the deformation volume under the indent to separate the unirradiated substrate contribution from that of the irradiated material. Another method is to indent the cross section of an ion-irradiated sample. Here, a hardness profile can be measured as a function of the ion irradiation damage profile [42]. This allows for a direct comparison between the bulk material properties and the irradiated material. An example of this method is shown in Figure 2.14.

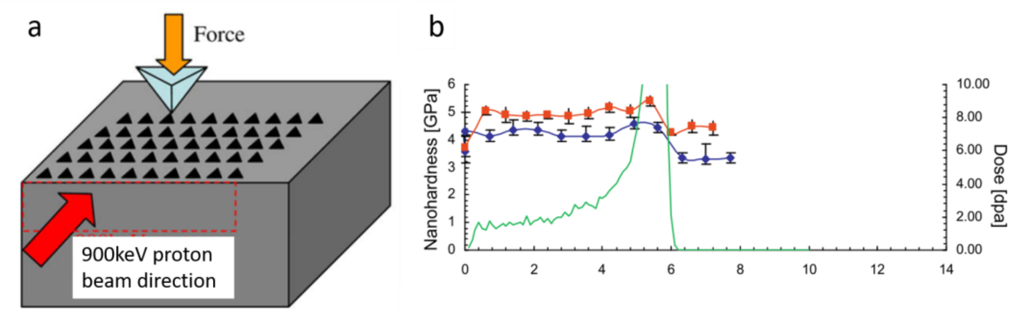

Figure 2.14 (a) Nanoindentation schematic on HT-9 alloy (b) nanoindentation results as a function of depth on proton irradiated HT-9 at room temperature with damage profile overlayed – adapted from [68]

In the study shown in Figure 2.14, Hosemann, et al, tested HT-9, an Fe-12%Cr alloy, irradiated with protons and helium ions at varying dose and temperature [68]. Hardness values increased with irradiation, while the magnitude of increase reduced with increased temperature [68]. Hosemann conducted a similar study on 304 stainless steel (SS) using 2 MeV protons to a dose of 10 dpa, with similar results – increase in hardness with irradiation [42].

Dolph, et al, conducted nanoindentation tests on an Fe-9%Cr alloy using 5 MeV Fe^{2+} ions at 400˚C. At a dose of 100 dpa, Dolph found strengthening of ~110-130 MPa [51]. This is half the strengthening mentioned previously in Section 2.1.3 for a similar alloy as predicted by microstructural changes. This difference in yield strength change can be accounted for in the higher temperature, 500˚C, in the material used in this thesis versus 400 ˚C used in ref [51].

Further reducing the sample volume and conducting nanoindentation using *in situ* TEM, could provide similar capabilities without the additional complications of an unirradiated substrate convoluting the analysis. Some of the drawbacks and complications with such a setup were discussed in ref. [69]. Knoop and Legros used both a pyramidal and wedge tip to indent Al on a Si film. They found that aligning the pyramidal indenter to the film was time-consuming and difficult, the wedge shape was much easier to align. They used a finite element model (FEM) to better understand the stresses seen throughout the film from the indentation [69]. Figure 2.15 shows their work. *In situ* TEM nanoindentation tests require additional work to understand if and how size effects would impact the results as well as the complications that may arise using more complicated alloys or irradiated materials.

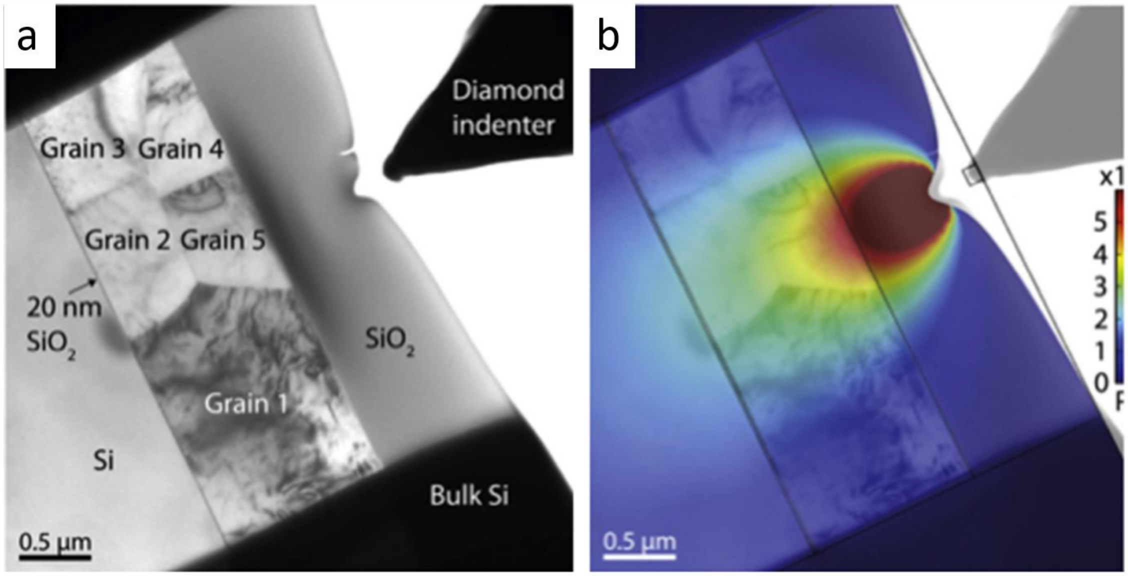

Figure 2.15 (a) *In situ* TEM nanoindentation on an Al film on Si (b) FEM von Mises stresses overlayed on TEM micrograph – adapted from [69]

Micro-tensile testing is ideal for measuring yield stress, elastic modulus, and ultimate tensile strength. *In situ* TEM tensile testing [33,70,71] and *in situ* SEM tensile testing [72] have been developed. In both cases, equipment such as a push-to-pull (PTP) system [72] or a tensile gripper microelectromechanical system (MEMS) device [33] must be utilized to conduct the testing. Figure 2.16 shows a PTP device in use. Prior work on this type of testing has combined the quantitative results from mechanical tests with qualitative results from *in situ* TEM imaging.

Micro-tensile testing also encounters size effects in pure metals, such as copper [33], and requires understanding of both the obstacle spacing, microstructural constraints, and the dimensional constraints as discussed in Section 2.1.3. Yet as discussed for conventional tensile testing in Section 2.3.1, Equations 2.15 and 2.16 can be used to evaluate yield strength and elastic modulus. Using the SEM or TEM imaging capability, important dimensions can be measured to calculate the cross-sectional area, *in situ* videos or displacement data can be used to calculate strain in the specimen, and the TEM holder MEMS device can measure the load applied.

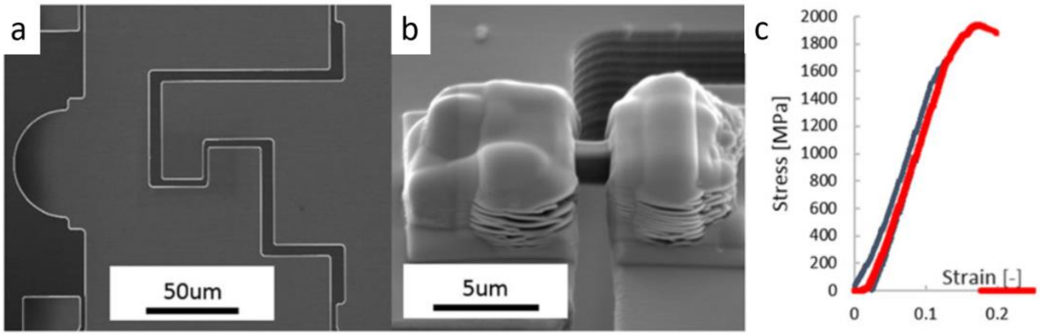

Figure 2.16 (a) SEM image of PTP device used for *in situ* TEM tensile testing (b) 10 dpa proton irradiated 304SS nano-whisker to be tested with PTP (c) resultant stress-strain curves – adapted from [42]

The work in Figure 2.16 was conducted by Hosemann on 304SS, irradiated with 2 MeV protons to a dose of 10 dpa. A yield strength of 1544 MPa was measured in the first test (gray). Fracture occurred in the second tensile test (red). Other work on micro-tensile samples includes observations of slip events in single crystal Ni [42] and Cu [71], observations of twin boundaries in Be [73], and tensile strengths and modulus of Co nanowires conducted *in situ* SEM [72]. Depending on the length scale and initial sample structure, sample preparation time varied from large amounts for FIB-prepared samples in [42] to quick placement of nanowires in [72]. Yet, micro-tensile testing allows for a direct analysis of fracture, unlike micro-compression testing which will be discussed in the next section.

2.3.3 Micro-Compression Testing

Micro-compression of pillars is one of the more prolific test methods and geometry used for *in situ* testing. The geometry is relatively easy to mill in a FIB and analysis for yield strength, elastic modulus, and qualitative information is straightforward. In this study, micro-compression pillar testing is the sole method used to evaluate size effects on mechanical properties in Fe-9%Cr. As such, a more detailed explanation of the methods used in this study will be included.

Micro-compression pillars are often made in a FIB machine. Both square [32] and cylindrical [38,42,74,75] geometries can be developed. Square geometries are favorable for having a reduced taper, yet cylindrical geometries are still used because they are easier to mill. Early studies compared the effect of square versus cylindrical geometries and as would be expected, found a wider range of yield strengths with an increase in taper angle due to the cylindrical geometry [43].

Generally, cylindrical pillars have been used for *in situ* SEM testing, where the pillars are milled directly into the bulk material. For *in situ* TEM, a lift-out can be made where the square pillar geometry is readily produced. This is well described in ref. [32] from which Figure 2.14 has been reproduced.

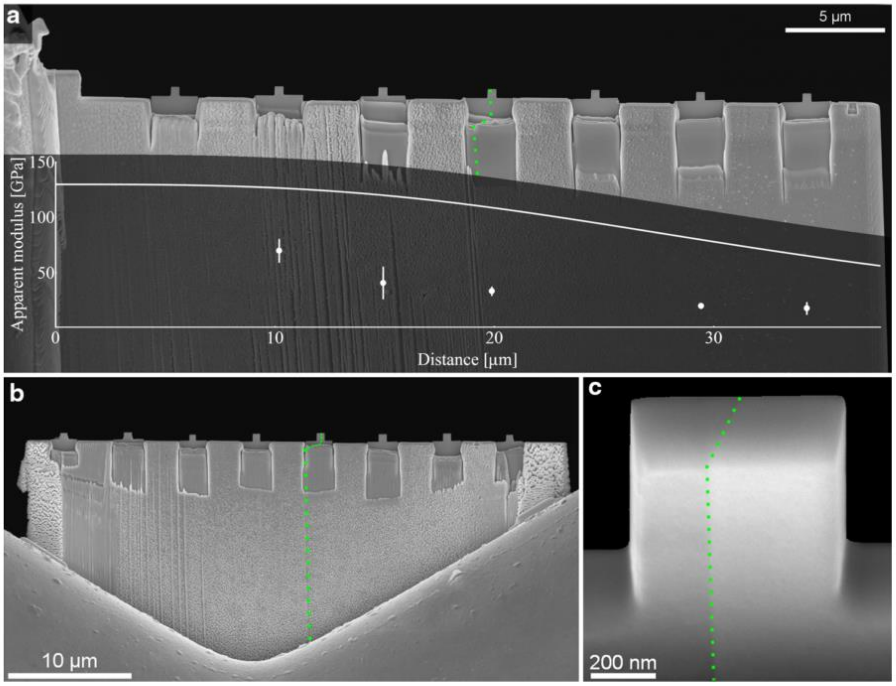

Figure 2.17 FIB lift-out with micro-compression pillars – reproduced from [32]

In the reproduced figure, one can see that multiple pillars can be milled out of a single lift-out and the rectangular geometry is highlighted in Figure 2.17c. In Figure 2.14b the ‘v’-shaped TEM grid post can be seen. In the work conducted in this thesis, the square TEM grid post was used instead to produce a more consistent modulus result through all the pillar samples across the lamella width. As discussed in ref [32], there were some adjustments needed to the modulus results due to their attachment design to the ‘v’-shaped grid post (Figure 2.17b) and single side attachment (Figure 2.17a) flexing under load. The FIB milling process used in this work will be discussed in more detail in Section 3.2.2.

Yield strength can be found by using the direct load-displacement data in combination with geometry dimensions measured *in situ* to produce stress-strain information [33,43,74]. The yield strength is generally found through the 0.002 strain offset method discussed previously in Section 2.1.4. Elastic modulus can be found during both the loading and unloading curve of the compression test. To account for any displacement in the pillar base, FEM have been incorporated into the analysis [32]. Again, Figure 2.18 below has been reproduced from Imrich, et. al [32].

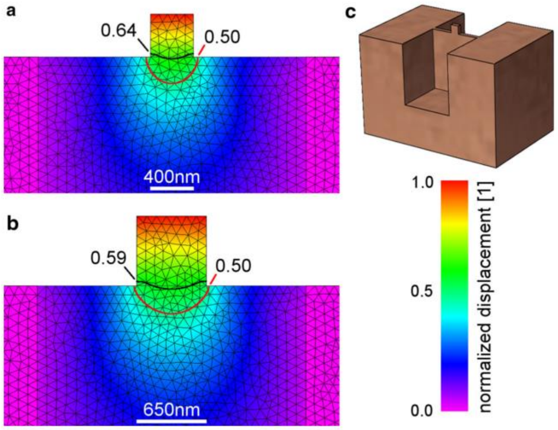

Figure 2.18 FEM for copper *in* situ TEM pillar compression testing showing normalized displacement in the pillar base – reproduced from [32]

By using Imrich's pillar design and lift-out method, this study also has a thin pillar base that deforms under load. However, using a finite element model to account for the deformation in the pillar base, we can adjust the resulting elastic modulus accordingly. In Figure 2.18, two samples, one 400 nm square (2.18a) and the other 650 nm square (2.18b), have been meshed with a triangular geometry and the displacement has been normalized. The black and red lines show the amount of displacement occurring below that line. In Figure 2.18a, 64% of the displacement takes place below the pillar. Likewise, 59% of the displacement occurs below the pillar in Figure 2.18b.

Our FEM used a 2D geometry of the various pillar and base sizes and normalized for the displacement as well. However, a quadrilateral mesh was used to improve accuracy. Material properties used in this FEM for Fe-9%Cr were taken were taken from [65] where a similar analysis was run to understand the plastic deformation zone for nanoindentation. More details on this model are discussed in Section 3.4.2.

In addition to testing only the ion irradiated layer, another major advantage of *in situ* TEM compression testing is the ability to correlate visual, qualitative events with quantitative mechanical results. *In situ* TEM testing provides an even closer look at qualitative microscale phenomena during mechanical testing; such as correlating dislocation motion or slip events with load drops or the onset of plasticity. *In situ* TEM potentially allows the observer to better understand the mechanisms involved with hardening and failure of a material under mechanical load. Slip events can be matched with load drops [76], dislocation motion can be followed and pinning obstacles can be identified [32], and twinning behavior can be observed [77]. There are still challenges with optimizing frame speed, load rates, and contrast conditions [32], but this technique uniquely allows for direct observation of the mechanisms leading to yield, hardening, and failure.

2.4 Size Effect in Microscale Mechanical Tests

As discussed previously in Section 2.1.3. there are microstructural constraints and dimensional constraints in a material. The microstructural constraints were described in detail along with their effect on mechanical properties in as received and irradiated conditions of Fe-9%Cr. The dimensional constraints will now be addressed, specifically in the context of being drawbacks to TEM/SEM *in situ* testing.

Size effects are seen when the dimensional constraints begin to reach the same scale as the microstructural constraints. Dimensional constraints are simply the specimen dimensions. In a bulk test this is on the order of millimeters. Any microstructural constraints in the material are found $\approx 10^3$ times over in that volume, suggesting that no size effects will be seen in those samples because the microstructure dominates the behavior in the material. Yet, in micro-mechanical testing, these dimensional constraints range from microns to nanometers – often the same order as the microstructural constraints. At this point, the dimensional constraints can begin to dominate the mechanical response of the material - a size effect is realized. For example, if the grain size is 200 nm, and the sample has a minimum dimension of 200 nm, then the average obstacle spacing in the microstructure cannot play a role in the yield strength. The specimen dimension dominates.

2.4.1 General Method to Resolve Size Effect

Prior studies have been conducted on micro-compression pillars to determine the impact of size effects on the yield strength. In general, a single dimension can be the limiting factor, e.g. thickness in a thin film [45] or the diameter of a pillar [41].

The general process to understand the interaction between microstructural and dimensional constraints, to in fact predict the presence of size effects in mechanical testing, is to first measure the obstacle spacing within the microstructure and compare that to the dimensions of the specimens to be tested. Obstacle spacing on the same order as the specimen dimensions will likely result in inflated yield strength values.

For single crystals, or simple microstructures, this obstacle spacing limit will be larger than the specimen dimensions used in an *in situ* SEM or TEM test. Yet with the addition of irradiation induced obstacles, the spacing may be reduced enough to allow smaller dimensioned specimens to be tested with valid and meaningful quantitative results. In fact, this was predicted by Hosemann in [42] as seen in Figure 2.19 below. This effect was also seen in irradiated copper in a study by Kiener, et al [41].

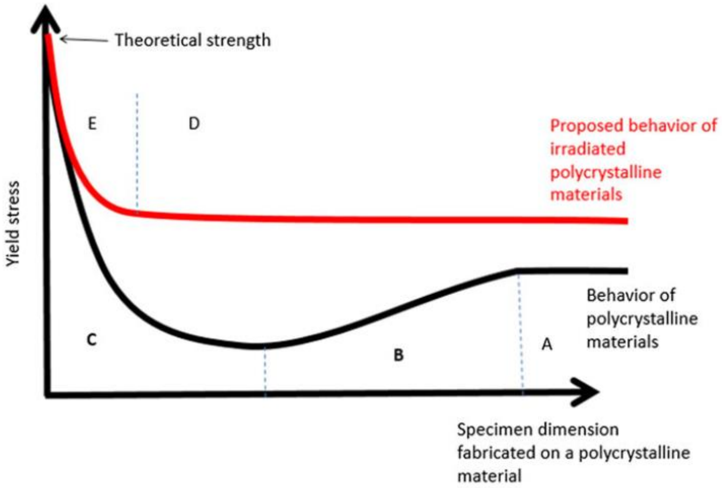

Figure 2.19 Size effect in unirradiated and irradiated polycrystalline materials – reproduced from [42]

Yet, for more complex alloys, irradiation is not always necessary to induce small enough obstacle spacing within the microstructure to result in meaningful measurements through *in situ* testing. In unirradiated Inconel MA6000, a Ni-based ODS alloy, a dimensional constraint of 2000 nm was seen in micro-pillar compression [39].

2.4.2 ODS Size Effect Factors

Due to the oxide dispersion, Fe-9%Cr has a small average obstacle spacing ranging between 17.2 and 33.7 nm. This allows the tested specimen dimensions to reach ≤100 nm before starting to see any size effect. Because the unirradiated condition has an even smaller obstacle spacing than the irradiated material, this dimensional constraint holds true for both conditions. This leads to the conclusion that the *in situ* TEM micropillar compression technique is valid for this material at minimum specimen dimensions above 100 nm.

Essentially, size effect comes down to a competition between two characteristics: the minimum dimension and the obstacle spacing on the glide plane [45]. This work simultaneously investigates both characteristics for Fe-9%Cr using *in situ* TEM micropillar compression and proves the validity of compressive yield strength measurements for the same technique at a minimum dimension above 100 nm.

CHAPTER THREE: TEM *IN SITU* MICROPILLAR COMPRESSION TESTS OF ION IRRADIATED OXIDE DISPERSION STRENGTHENED ALLOY

3.1 Introduction

Ion irradiation is increasingly being used to scope long-term, high irradiation damage dose behavior of advanced nuclear reactor candidate materials. Characterizing the irradiation evolution of mechanical properties is challenging, however, because ion irradiation produces a near-surface damage layer on the order of a few hundred nm to a few tens of microns. Logically, small-scale mechanical tests have been utilized on ion irradiated materials, including nanoindentation [40,63,64,78–80], SEM *in situ* pillar compression [66], and cantilever bend tests [40]. However, it remains difficult to isolate the mechanical performance of the ion irradiated layer from that of the unirradiated substrate. TEM *in situ* mechanical testing may be a viable alternative technique for evaluating the mechanics of ion irradiated layers because it is capable of analyzing even smaller sized specimens than nanoindentation and SEM *in situ* approaches.

A common concern, however, with TEM *in situ* mechanical testing is the sample size effect, in which the extremely miniaturized specimen size – rather than the dispersion of microstructural obstacles to dislocation motion – controls deformation behavior. As such, TEM *in situ* specimens below a size threshold often exhibit mechanical properties that deviate significantly from bulk values. However, recent work [41] has suggested that the high number density of irradiation-induced microstructural features reduces the size threshold.

We focus this study on a model ODS alloy, which is a candidate material for structural and cladding components in advanced nuclear fission reactors and fusion first-wall applications. ODS alloys have a fine dispersion of oxide nanoclusters, which serve as a preexisting high number density of microstructural features. As is common for ion irradiation experiments, we irradiate a bulk specimen of the ODS alloy. This presents a unique set of challenges in the post-irradiation fabrication of TEM *in situ* specimens.

The objective of this study is to assess the validity of utilizing TEM *in situ* micropillar compression tests to quantitatively measure mechanical properties of as received and ion irradiated model Fe-9%Cr ODS alloy. We fabricate micropillars of varying dimensions so as to observe the dependence of mechanical properties on pillar volume and pillar minimum dimension. We measure the yield stress and elastic modulus from each micropillar compression test. A finite element model provides a two-dimensional visualization of the development of plasticity through the pillars and their base material. Finally, TEM and APT characterize the irradiated microstructures, which correlate well with the measured irradiation-induced changes in yield stress. This work also presents a versatile specimen fabrication method for TEM *in situ* mechanical testing of irradiated bulk materials.

3.2 Experiments

3.2.1 Material and Irradiation

A rod of Fe-9%Cr ODS martensitic steel material (composition provided in Table 2.1) was provided by the Japan Nuclear Cycle Development Institute (now known as the Japan Atomic Energy Agency). The rod was processed by mechanically alloying ferritic steel with Y_2O_3 powders, then hot extruding at 1150°C. Finally, the rod was heat treated at 1050°C for 1 hour, air cooled, then tempered at 800°C with subsequent air cooling. Additional details regarding the mechanical alloying and fabrication of the rod are available in ref. [47].

Specimens are first prepared for bulk ion irradiation by electrical discharge machining into 1.5 mm × 1.5 mm × 16 mm bars. Each bar is mechanically polished through 4000 grit SiC paper, followed by electropolishing for 20 seconds in a 10% perchloric acid + 90% methanol solution maintained between -30°C and -40°C, with a 35 V applied potential between the specimen (anode) and platinum mesh cathode. The specimens are subsequently irradiated with 5.0 MeV Fe^{2+} ions to doses of 3 displacements per atom (dpa) or 100 dpa at 500°C using a 1.7 MV General Ionex Tandetron accelerator at the Michigan Ion Beam Laboratory. The beam is rastered at 255 Hz. A combination of resistance heating and air cooling are used to maintain the irradiation temperature at 500±10°C at high vacuum pressures below 1.3×10^{-5} Pa (10^{-7} torr). Beam current is recorded throughout the duration of the experiment to ensure accurate dose accumulation. The irradiation dose rate is $\sim 10^{-4}$ dpa/s.

The displacement damage profile for 5.0 MeV Fe^{2+} ions normally incident on Fe-9%Cr is calculated using the SRIM 2013 program in “Quick Calculation” (Kinchin-Pease) mode [31] and displacements are obtained from the vacancy.txt file. The damage profile (Figure 3.1) exhibits a steep gradient between the surface and the damage peak, which is located approximately 1.2 µm from the surface. The target irradiation dose of 50 dpa is achieved at a depth of 550 nm from the surface, which avoids both the surface sink and the Fe implantation peak.

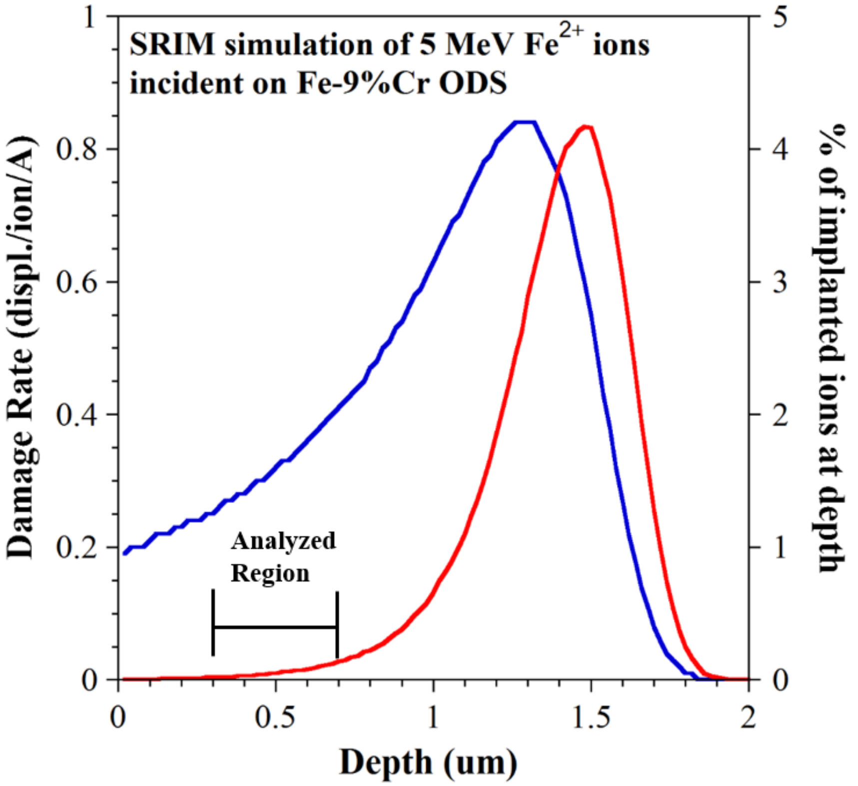

Figure 3.1 **SRIM 2013** [31] **calculation of damage profile for 5 Mev Fe^{2+} ion irradiation normal to Fe-9%Cr in "quick calculation" mode**

3.2.2 Sample Preparation

TEM mechanical testing of irradiated materials in the archival literature [41] has been conducted on miniaturized specimens first milled by FIB, then subsequently ion irradiated (generally in an *in situ* FIB or TEM environment). However, since ion irradiation is more commonly performed on bulk materials, preparing miniaturized specimens for TEM mechanical testing subsequent to the irradiation, presents a new challenge. Here, we modify previous sample preparation methods published by Imrich [32] and Legros [69] to utilize FIB machining to fabricate a TEM lamella containing multiple compression pillar specimens for TEM *in situ* mechanical testing. This technique can also be utilized to create indentation "window" specimens for TEM *in situ* mechanical testing, although these windows will not be tested or analyzed in this paper.

The versatility of this technique enables it to be utilized effectively for both irradiated and unirradiated specimens. All FIB work herein is conducted on an FEI Quanta 3D FEG FIB at the Center for Advanced Energy Studies (CAES).

We first adhere a three-pillar copper TEM half grid to the copper sample mount using conductive silver epoxy (Figure 3.2). The nano-sized dimensions of the ODS and small loads limits the amount of stress in the copper grid and epoxy to < 0.015% of the stress seen in the ODS. Hence we can assume no deformation is occurring in the copper grid and silver epoxy.

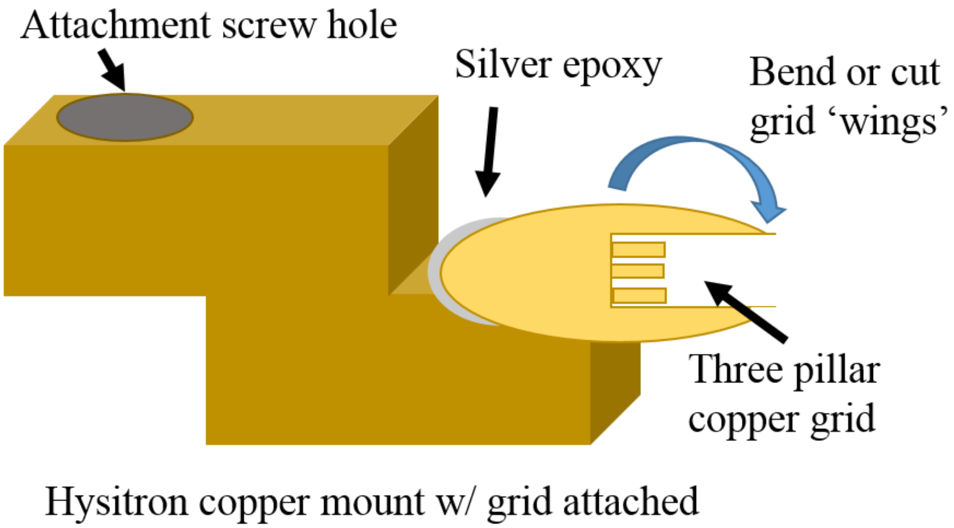

Figure 3.2 Diagram showing the TEM copper half-grid attached with silver epoxy to the hysitron copper mount

A lamella having approximate dimensions 40 µm × 20 µm × 3 µm is lifted normal to the irradiated surface using focused ion beam (FIB). Throughout this procedure, the FIB operating voltage is maintained at 30 kV, while the current is varied at each step to control the precision of each cut. The irradiated surface is first protected depositing a 40 µm × 3 µm × 0.8 µm platinum strip over the area of interest using a 0.3 nA beam current. The lamella is then lifted following the conventional FIB lift-out technique for

TEM specimens [81], using trenching around the platinum strip, freeing the lamella from the bulk, and finally, lifting the lamella using an Omniprobe needle.

The lamella is then affixed to the TEM half-grid on the center post, which simplifies alignment of the indenter tip to the compression pillar or indentation window. Before attaching the lamella to the grid, the center grid post is milled to create a straight edge >40 μm wide. The lamella is then aligned such that its lower third overlaps the post before it is brought into slight contact with the post. Subsequently, a platinum weld is made across the bottom length of the lamella (Figure 3.3a), after which the lamella is detached from the omniprobe. Next, the stage is rotated ±45° and fillet welds are placed along each side of the lamella (Figure 3.3b). A top-down view of all three welds is shown in Figure 3.3c. After the lamella is securely welded to the grid, the entire sample mount is installed onto a pre-tilted 45° stage to allow for perpendicular milling of the lamella surface to shape the microscale compression pillars.

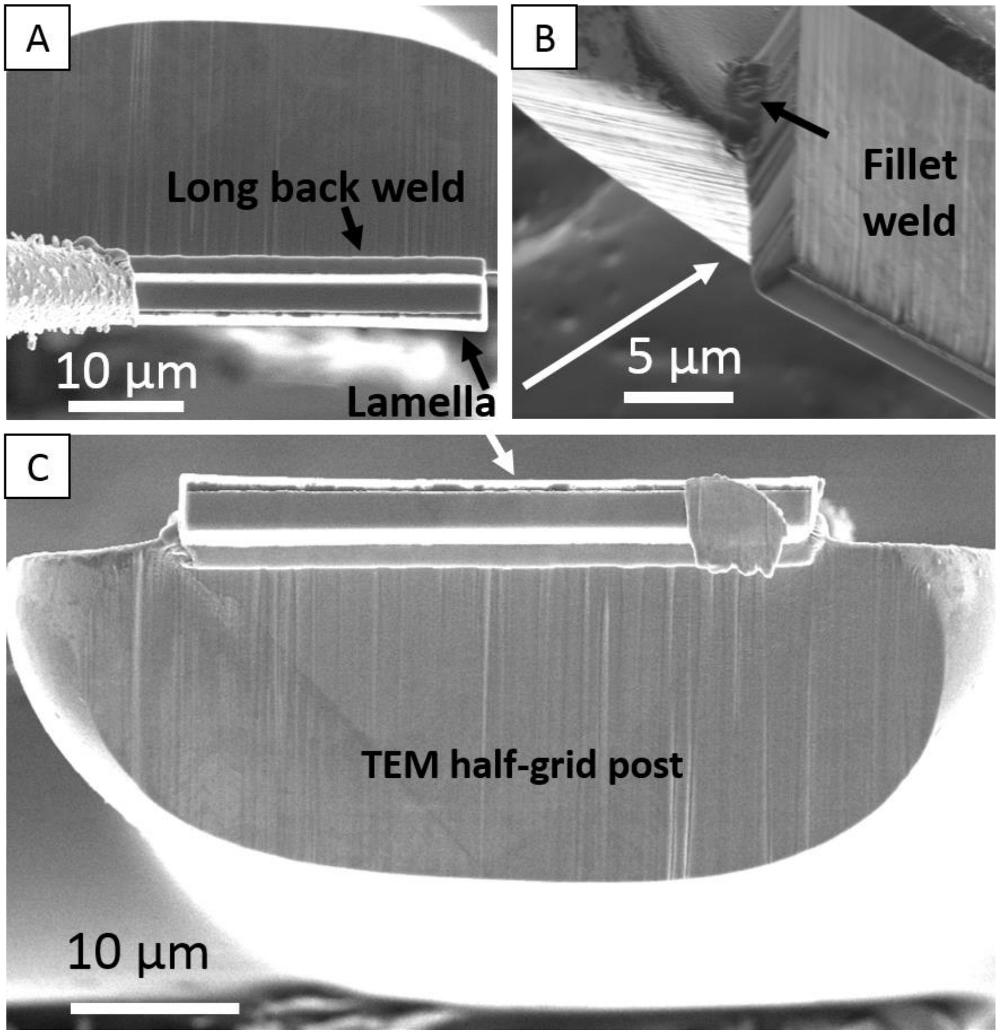

Figure 3.3 SEM images showing (A) overlap of the lamella on the TEM half-grid post with weld across the bottom edge of the lamella, (B) fillet weld along sides of lamella at 45°, and (C) the three welds used to attach the lamella to the TEM half-grid post

Pillars are fabricated with rectangular (as opposed to circular) cross-sections to reduce the extent of taper along the pillar height, simplifying the evaluation of mechanical properties [76,82]. Indentation windows, if made, should be electron transparent to enable observation of dislocation movement during indentation. Ideal geometries of both windows and pillars are shown in Figure 3.4a.

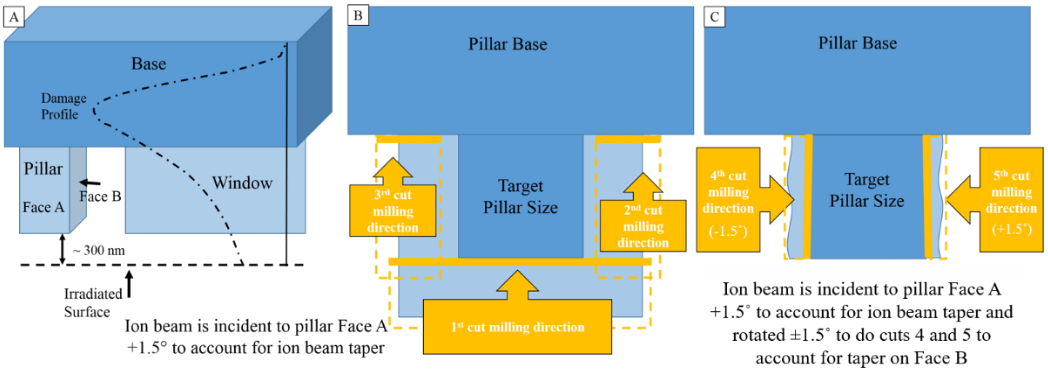

Figure 3.4 (A) Ideal pillar and window geometries with SRIM damage profile for 5 MeV Fe^{2+} overlaid; (B) first three cuts to shape pillar, with milling direction indicated; (C) the fourth and fifth cuts clean up B faces of the pillar to final desired dimensions

Each pillar and window is shaped to position its top surface ~300 nm below the original irradiated surface such that the entire testing volume is located within the ion irradiated region. This configuration also avoids any surface oxidation and sputtering effects of irradiation. The sample preparation technique presented here accommodates 6-8 micro-compression pillars and/or indentation windows on a single TEM lamella, spaced 2-2.5 µm apart. Once the locations for pillars and windows are identified, excess material between these locations are removed (Figure 3.5a) at a current of 1 nA to ensure the indenter tip does not accidentally contact this excess material during testing. The sample is rotated normal to the ion beam, then tilted +1.5° to account for ion beam spreading. Sites of interest are now ready for thinning into windows or shaping into pillars.

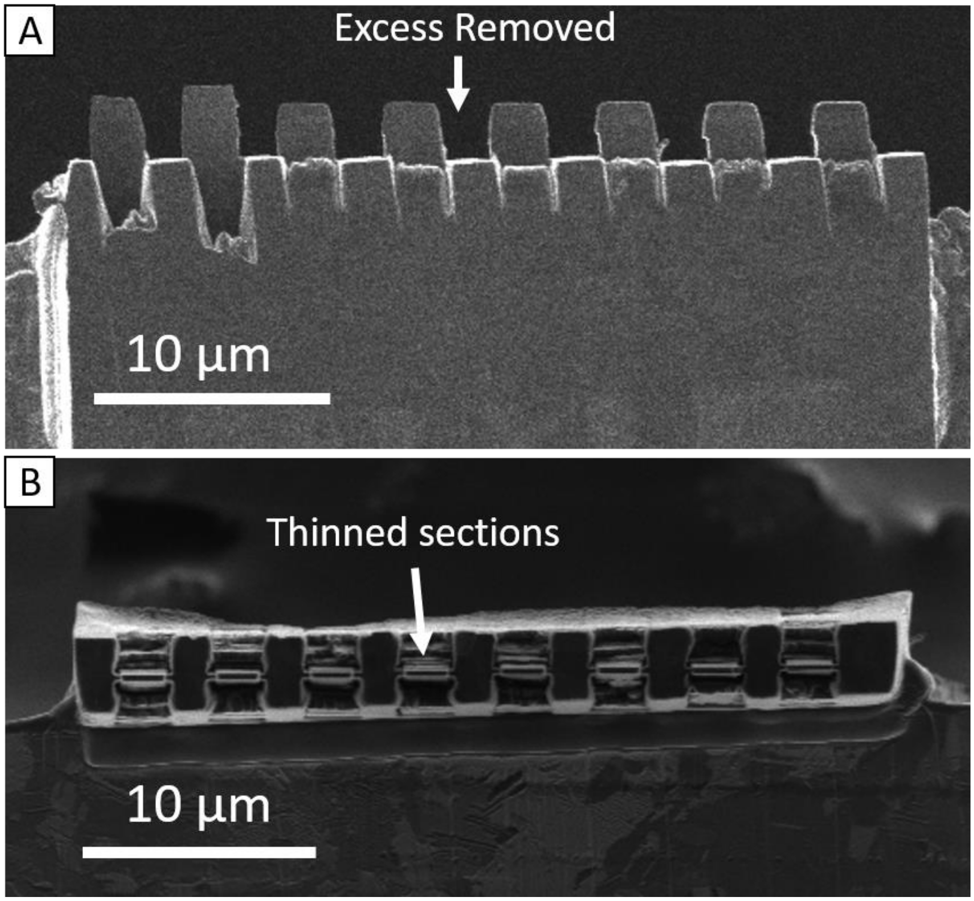

Figure 3.5 SEM images showing (A) side view of excess material removed between pillar or window sites, and (B) top view of pillar or window sites thinned to target thickness

Window sites need no further shaping, and can simply be thinned to electron transparency. Pillar sites, however, are first thinned to the target thickness before the subsequent shaping process. Thinning proceeds after rotating the sample 180° and tilting such that the ion beam is parallel to the lamella (incident on the irradiated surface). Cleaning cuts are made with progressively decreasing ion beam currents, beginning with 0.3 nA and decrementing to 10 pA for final thinning. Targeted pillar thicknesses vary from 150 nm to 600 nm at the nominal dimensions with the quantity tested shown in Table 3.1, while window thicknesses are <100 nm to ensure electron transparency. It is imperative to not thin so deep as to compromise the weld along the reverse side of the lamella; a depth of 0.1 µm is used. Figure 3.5b illustrates a sample thinned to the target thickness.

Table 3.1 Quantity tested of targeted nominal pillar dimensions

Width and Height (nm)		Thickness (nm)								
		100	**150**	**200**	**250**	**300**	**350**	**400**	**500**	**600**
As Received	**150**	–	1	–	–	–	–	–	–	–
	200	1	–	1	–	–	–	–	–	–
	250	–	–	–	1	–	–	–	–	–
	300	1	–	–	–	1	–	–	–	–
	350	–	–	–	–	–	1	–	–	–
	400	2	–	1	–	1	–	2	–	–
	500	1	–	–	–	–	–	–	1	–
	600	–	–	1	–	–	–	–	–	1
Width and Height (nm)		Thickness (nm)								
		100	**150**	**200**	**250**	**300**	**350**	**400**	**500**	**600**
Fe^{2+} Irradiated ODS 3 dpa 500°C	**150**	–	1	–	–	–	–	–	–	–
	200	1	–	–	–	–	–	–	–	–
	250	–	–	–	1	–	–	–	–	–
	300	–	–	–	–	2	–	–	–	–
	350	–	–	–	–	–	–	–	–	–
	400	2	–	1	–	–	–	1	–	–
	500	1	–	–	–	–	–	–	1	–
	600	–	–	–	–	–	–	–	–	2
Width and Height (nm)		Thickness (nm)								
		100	**150**	**200**	**250**	**300**	**350**	**400**	**500**	**600**
Fe^{2+} Irradiated ODS 100 dpa 500°C	**150**	–	1	–	–	–	–	–	–	–
	200	–	–	1	–	–	–	–	–	–
	250	–	–	–	1	–	–	–	–	–
	300	–	–	–	–	1	–	–	–	–
	350	–	–	–	–	–	–	–	–	–
	400	5	–	–	–	1	–	1	–	–
	500	–	–	–	–	–	–	–	–	–
	600	–	–	–	–	–	–	–	–	1

Once thinned, pillars are shaped to the target dimensions using cleaning cross-section cuts at 10 pA. The sample is rotated incident on face A (as identified in Figure 3.4a) of the pillar. These shaping cuts remove what remains of the protecting platinum layer. For cuts milled in the direction of irradiated surface (Figure 3.4b), the sample is over-tilted by +1.5° to account for taper. When shaping from the B faces of the pillar, the sample is also rotated ±1.5° to keep the pillars as square as possible (Figure 3.4c). Completed pillars and windows are shown in Figure 3.6. It is important to note that while we show that window preparation is easily attained using this process, window indentation testing and analysis is not considered in this manuscript.

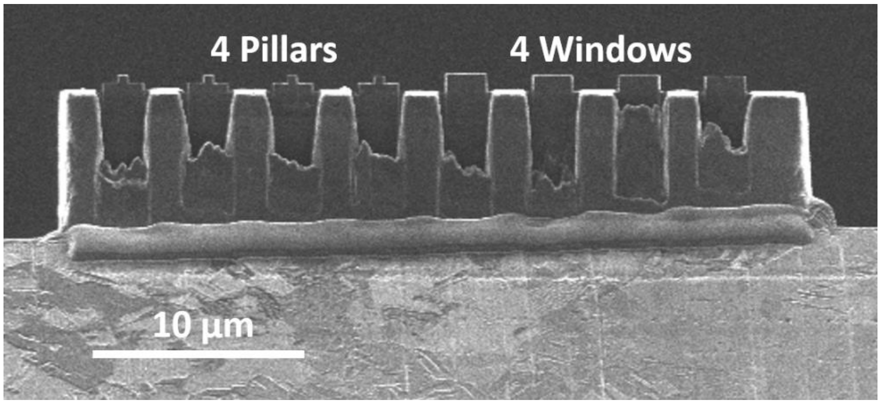

Figure 3.6 SEM side view image of completed lamella containing four pillars and four indentation windows

3.2.3 TEM *In Situ* Mechanical Testing

In situ mechanical testing is conducted using a Hysitron PI95 Picoindenter in an FEI Tecnai TF30-FEG STwin scanning transmission electron microscope (STEM) at CAES. Hysitron TriboScan software is used to conduct tests and collect load-displacement data and video; the frame grabber is used to capture the TEM charge coupled device (CCD) screen output. In this study, pillars are tested from both Fe^{2+} irradiated specimens (3 dpa and 100 dpa at 500°C); the as received material is also tested as a control.

All pillar compressions tests are conducted in displacement-controlled mode using a flat punch diamond tip. Displacements are defined as half the height of the original pillar to ensure yielding and plastic deformation. To reduce system creep, the load time is set to 20 seconds with a 5 second hold time and 10 second unload time. Displacement depths vary from 50-125 nm using a three-segment loading curve defined with a 20 second load period, 5 second hold period, and 20 second unload period. Varying the displacement depth enables one to produce deformation in varying regions of the window to observe deformation at specific microstructural features. Video compression settings are optimized for size and quality to MJPEG compression at 30 frames per second and 0.15 second exposure.

3.2.4 Microstructure Characterization

TEM analysis is conducted to evaluate microstructure evolution under self-ion irradiation. TEM lamellae are prepared from the as received and ion irradiated specimens using the FIB lift-out technique [81] on an FEI Quanta 3D FEG FIB at CAES. Lamellae are oriented perpendicular to the irradiated surfaces, providing a cross-section of the irradiation damage profile within the TEM film. Prior to milling, all specimen surfaces are protected with a 3 µm platinum deposit to ensure that the original surface is retained for reference. Each sample is milled at 30 kV to approximate dimensions of 15 µm × 7 µm × 100 nm. The samples are subsequently milled at 5 kV to an estimated thickness of 50-100 nm, followed by cleaning at 2 kV for approximately 1 minute on each side to reduce FIB-induced surface damage.

Microstructure analysis focuses on characterizing the size and number density of grains, dislocations, carbide precipitates, voids, and dislocation loops. The analyzed region is within 300 – 700 nm from the surface and the microstructural data is averaged over this entire depth. TEM specimens are analyzed using an FEI Tecnai TF30-FEG STEM at CAES. Grains and carbides are imaged in bright field mode. Voids (when present) are imaged in bright field mode using the through-focus technique [83]. Dislocation line density is determined by measuring the linear density of dislocations in perpendicular directions and calculating an effective area density. Dislocation loops are imaged in STEM mode following a procedure outlined by Parish et al. [83] in which small collection (β) and convergence (α_{CON}) angles are applied to create a STEM bright field image. For loops imaged close to an "edge-on" condition, the longer dimension observed is taken to be the loop diameter [84]. Oxide nanoclusters are imaged in bright field mode in areas with low dislocation contrast so that the z-contrast of the oxides is more apparent. A limitation of this technique, however, is that nanoclusters $\lessapprox$2 nm in diameter are difficult to resolve [83]. Thus, APT is used to complement the TEM analysis by enabling atomic-resolution characterization. Finally, the specimen thickness is measured with electron energy loss spectroscopy (EELS). Image collection and analysis is conducted using Digital Micrograph software. Additional details regarding the TEM sample preparation and analysis may be found in reference [23].

Needles for APT are fabricated by FIB milling and are analyzed using a Cameca LEAP 4000× HR at CAES, operated in laser pulsed mode with samples maintained at 40 K. Laser power ranges from 40-70 pJ with a pulse repetition rate of 200 kHz. Each data set is reconstructed with the Integrated Visualization and Analysis Software (IVAS) Version 3.6.2 using a SEM image of the needle profile and a tip radius between 3-10 nm. Each tip rendering is visually inspected to ensure the tip volume is consistent with the SEM image, and that the existing cluster morphology is consistent with that observed via TEM.

Cluster analysis is performed on each tip (excluding those volumes attributed to carbides or grain boundaries) using the maximum separation method [85] with the cluster analysis module within IVAS. Appropriate d_{max} and N_{min} values are selected for each condition following the approach proposed by Kolli and Seidman [86] and further refined by Williams, et al. [87], in which the selected d_{max} yields a minimum number of counted clusters by the analysis. Once the parameters are selected, a visual inspection of each cluster rendering confirms the identified clusters are consistent with those observed in the original APT reconstruction.

The IVAS cluster analysis output file provides values for R_{gx}, R_{gy} and R_{gz} for each cluster, which are taken to be the respective radii of gyration in each coordinate direction. An overall radius of gyration (R_g) for each cluster is calculated according to [88]:

$$R_g = \sqrt{R_{gx}^2 + R_{gy}^2 + R_{gz}^2}$$

Equation 3.1

and the Guinier diameter (D_G) for each cluster is determined using [88,89]:

$$D_G = 2\sqrt{\frac{5}{3}}R_g$$

Equation 3.2

The average and standard deviation is calculated over all measured clusters, and the error propagation formula is used to calculate an overall standard deviation for the Guinier diameter. The standard deviation of the mean is also calculated to evaluate the relative certainty of the mean diameter. The cluster number density (N_{nc}) is determined by:

$$N_{nc} = \frac{\sum N_c}{\sum V_T}$$

Equation 3.3

where ΣN_c is the total number of clusters identified in all tips from a given condition and ΣV_T is the total analyzed volume in all tips from that condition. Additional details regarding the APT sample preparation and analysis may be found in reference [23].

3.3 Results

3.3.1 Pillars

In this work, three material conditions are studied, and in each condition, pillars are fabricated with various dimensions to evaluate dependencies on thickness, width/height, and total volume. Size effects have been observed at minimum diameters [41], and the experiment plan (Table 3.1) enables us to determine whether size effects are present herein. Pillars range 50 nm – 600 nm in thickness, 100 nm – 600 nm in width and height, with total volumes ranging 2.5 μm^3 - 246 μm^3.

An advantage of *in situ* TEM mechanical testing is the ability to simultaneously collect load-displacement data and TEM resolution video of deformation. By analyzing these data side-by-side, one can obtain a fundamental understanding of plasticity, slip, and relative strengths of obstacles to dislocation motion. Frames from an *in situ* TEM compression test of a 400 nm × 400 nm × 100 nm pillar in the as received condition have been extracted from the video recording and are shown in Figure 3.7. Corresponding points in the stress-strain curve are identified for each image. Before compression (Figure 3.7a), the pillar contains no grain boundaries but does contain characteristic ODS oxides and dislocations interspersed. After yielding, plasticity occurs in large dislocation burst events (3.7c and 3.7d). The test concludes with a highly deformed pillar containing a dense network of dislocations (3.7e).

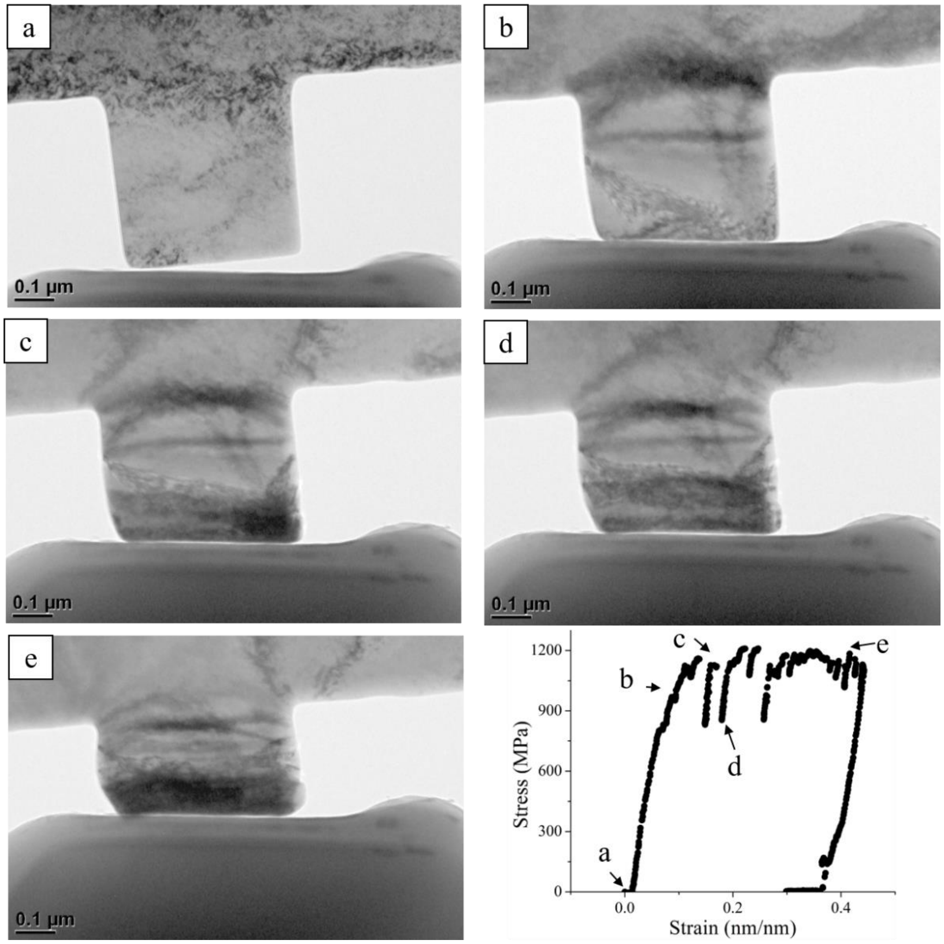

Figure 3.7 ***In situ*** **compression test of as received ODS 400 nm × 400 nm × 100 nm pillar. (a-e) show pillar condition at each labeled point in stress-strain curve. dislocation bursts are observed at (c) and (d), representing load drops observed on stress-strain curve**

Pillar dimensions are measured from EELS and using Digital Micrograph software. A stress-strain curve is generated from the load-displacement data collected during each pillar test. As there is deflection in the base material of the pillar, we must subtract this maximum deflection (acquired from the real-time video of the compression tests) from the transducer displacement data before calculating the strain. The effect of this subtraction is further examined in the Discussion section below. Yield strength and elastic modulus are extracted from these stress-strain curves. Representative curves are shown in Figure 3.8 for each material condition. The nominal dimensions of these representative samples are as follows: as received – 500 nm × 500 nm × 500 nm, 3 dpa 500°C – 600 nm × 600 nm × 600 nm, 100 dpa 500°C – 400 nm × 400 nm × 400 nm. Measured yield strengths from all pillars tested are shown in Figure 3.9; averages are reported in Table 3.2.

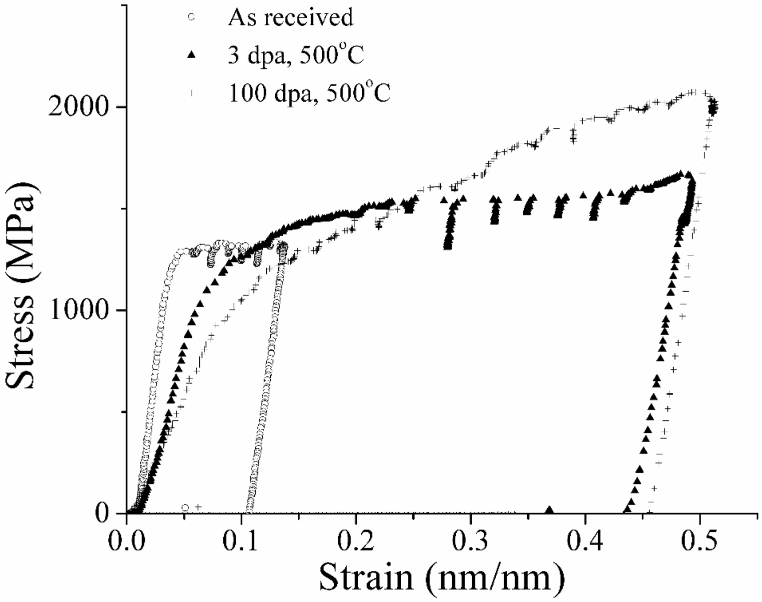

Figure 3.8 Representative stress strain curves from the as received, 3 dpa, and 100 dpa conditions. the nominal dimensions of these representative samples are as follows: as received – 500 nm × 500 nm × 500 nm, 3 dpa 500°C – 600 nm × 600 nm × 600 nm, 100 dpa 500°C – 400 nm × 400 nm × 400 nm

Table 3.2 Yield strength measurements from compression pillars

		As Received	**Fe^{2+} Irradiated 3 dpa, 500°C**	**Fe^{2+} Irradiated 100 dpa, 500°C**
All	Average yield strength (MPa)	1269 ± 256	1245 ± 294	1188 ± 217
	# of pillars	15	13	12
Minimum dimension <100 nm	Average yield strength (MPa)	1014 ± 83	1266 ± 383	1250 ± 293
	# of pillars	4	5	5
Minimum dimension >100 nm	Average yield strength (MPa)	1362 ± 233	1233 ± 221	1145 ± 125
	# of pillars	11	8	7

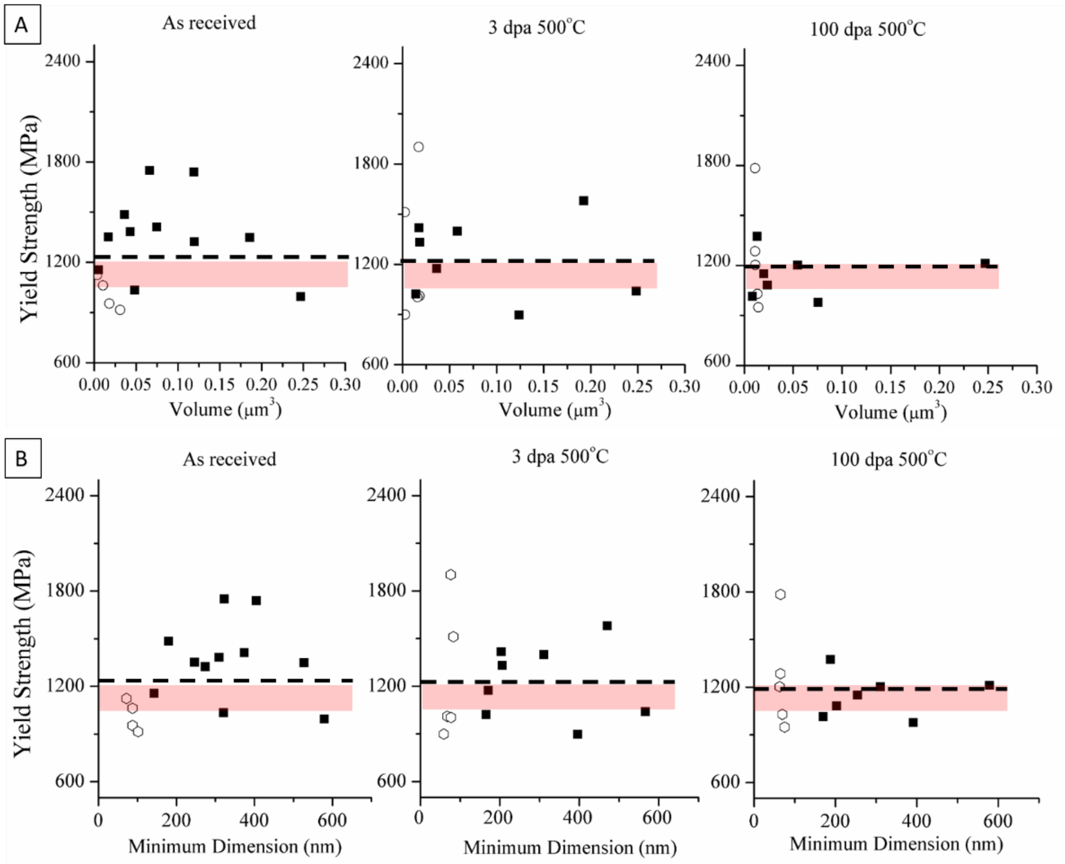

Figure 3.9 Measured yield strength as a function of (A) pillar volume or (B) minimum pillar dimension. Open symbols represent pillars having minimum dimension <100 nm; closed symbols represent pillars having minimum dimension >100 nm. Dashed line represents the average of measurements; shaded band represents expected values

The expected yield strength for as received Fe-9Cr ODS is 1000-1200 MPa [59]. Within the 95% confidence interval, 9 of 15 pillars tested exhibit yield strengths in this expected range. We measure an average reduction in yield stress of ~129 ± 321 MPa in the 3 dpa condition and ~217 ± 264 MPa in the 100 dpa condition (Figure 3.9). These differences were calculated using the average yield strength of pillars with a minimum dimension greater than 100 nm and propagating the uncertainty in quadrature. The standard deviations being on the same order as the yield stresses suggests statistical invariance between conditions. Dolph, et al. [65] observed minimal strengthening (~110-130 MPa) in the same alloy irradiated to 100 dpa at 400°C, which is reasonable given the higher irradiation temperature of the specimens studied herein. A possible size effect is also observed for pillar thicknesses below ~100 nm (Figure 3.9), which are identified by open symbols, while pillars having minimum dimension >100 nm are depicted with closed symbols.

The expected elastic modulus for as received ODS ranges 190-220 GPa [51,59,65]. Yet the values measured by *in situ* TEM compression pillars (Figure 3.10, Table 3.3) are an order of magnitude lower. This discrepancy is attributed to two factors. First, deformation is not isolated in the pillar; the base also deforms [32]. The acquired load-displacement curve does not adjust for the deformation in the base, resulting in lower elastic modulus measurements. It also follows that as the pillar volume increases (here highlighted by the thick vs thin samples), more of the deformation can be accommodated in the pillar than in the base, resulting in more consistent modulus measurements (Figure 3.10b). Secondly, in such small volumes, the elastic modulus can be significantly affected by microstructural inhomogeneities such as varying grain orientations and distribution of oxide nanoclusters. These factors will be discussed in greater detail in Section 3.4.2.

Table 3.3 Elastic modulus measurements and adjustments from compression pillars

	As Received	**Fe^{2+} Irradiated 3 dpa, 500°C**	**Fe^{2+} Irradiated 100 dpa 500°C**
Number of pillars	15	13	12
Measured elastic modulus (GPa)	40.8 ± 15.3	34.4 ± 15.3	25.4 ± 6.8
Deflection adjusted elastic modulus (GPa)	112 ± 92.0	41.7 ± 18.0	51.1 ± 12.4
Deformation adjusted elastic modulus (GPa)	253 ± 209	174 ± 74.8	213 ± 51.6

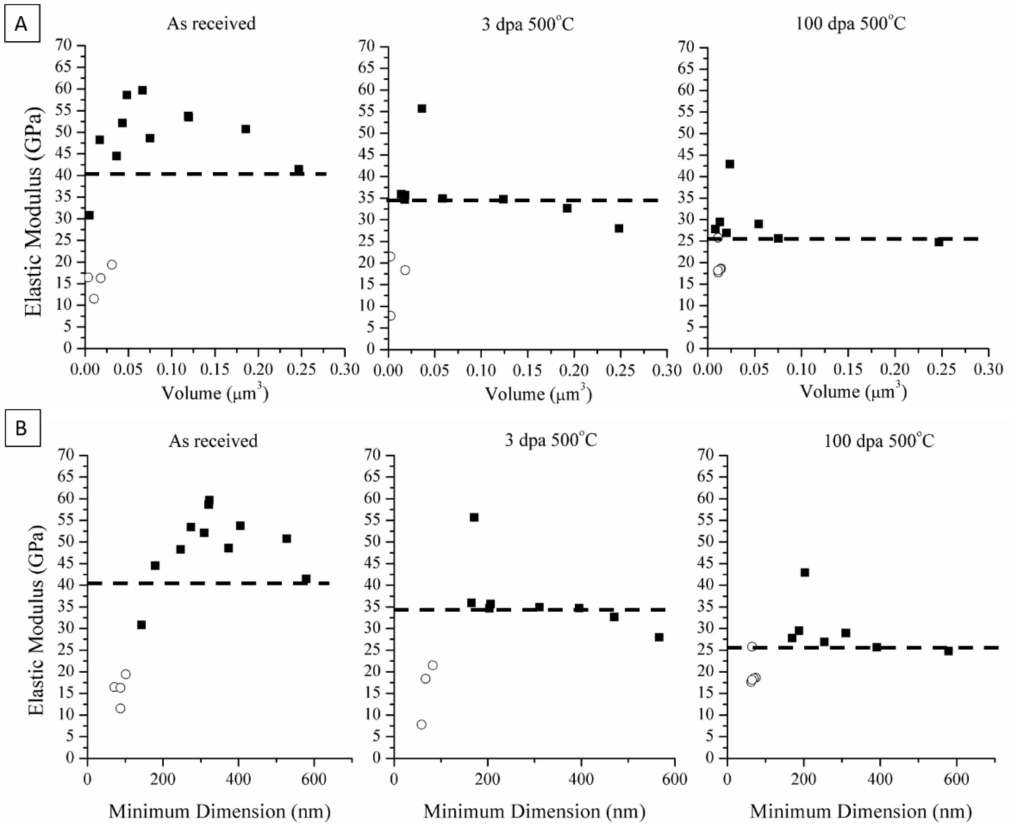

Figure 3.10 Measured elastic modulus as a function of (A) pillar volume or (B) minimum pillar dimension. Open symbols represent pillars having minimum dimension <100 nm; closed symbols represent pillars having minimum dimension >100 nm. Dashed line represents the average of measurements

TEM *in situ* compression pillars provide relatively consistent yield stress measurements as bulk techniques for both unirradiated and irradiated samples as was seen in Kiener's work [41]. Conversely, direct elastic modulus measurements are much lower than bulk values and other considerations must be accounted for.

3.3.2 Microstructure

In the specimens irradiated to 3 dpa and 100 dpa, average grain sizes range 0.28-0.37 μm and average carbide sizes are consistent at 0.08 μm. Carbide number densities range 0.29-0.76 × 10^{20} m^{-3}, and dislocation line density varies over 18.4-22.6 × 10^{14} m^{-2}. These features are statistically invariant from those in the as received condition, reported in reference [23] and summarized in Table 3.4. Voids are not distinctly observed in any of the ion-irradiated specimens. Irradiation-induced dislocation loops are imaged in STEM mode [83] on the [111] zone axis, and loop orientation maps [84] are used to determine whether the loops reside on the {111} or {001} habit plane (Figure 3.11). Loops produced by Fe^{2+} irradiation to 3 dpa and 100 dpa have average diameter 8.5 ± 2.2 nm and 10.7 ± 4.2 nm, respectively, and number densities of $2.1 \pm 0.1 \times 10^{21}$ m^{-3} and $4.3 \pm 0.8 \times 10^{21}$, respectively. Representative atom distribution maps from the APT analysis are shown in Figures 3.12 and 3.13 for specimens irradiated to 3 dpa and 100 dpa, respectively.

Table 3.4 Summary of microstructural measurements; as received data reprinted from ref. [23]

Feature	**Measurement**	**As received**	**Fe^{2+} irradiated (3 dpa, 500°C)**	**Fe^{2+} irradiated (100 dpa, 500°C)**
Grains/Laths	# of grains measured	104	104	105
	Effective diameter ($\times 10^{-6}$ m)	0.23 ± 0.12	0.28 ± 0.08	0.37 ± 0.19
Dislocation lines	# of measurements	17	21	35
	Density ($\times 10^{14}$ m^{-2})	19.1 ± 3.8	22.6 ± 4.8	18.4 ± 6.9
Carbide Precipitates	# of carbides measured	36	48	34
	Effective diameter ($\times 10^{-6}$ m)	0.11 ± 0.07	0.08 ± 0.04	0.08 ± 0.03
	Density ($\times 10^{20}$ m^{-3})	0.20	0.76	0.29
Dislocation loops	# of loops measured	0	48	182
	Diameter ($\times 10^{-9}$ m)	–	8.5 ± 2.2	10.7 ± 4.2
	Density ($\times 10^{21}$ m^{-3})	–	2.1 ± 0.1	4.3 ± 0.8
Oxide nanoclusters	# of nanoclusters measured	486	232	1578
	Diameter ($\times 10^{-9}$ m)	5.96 ± 3.10	5.06 ± 2.0	5.35 ± 2.80
	Density ($\times 10^{21}$ m^{-3})	568	171	513
Average obstacle spacing on glide plane (nm)		17.2	33.7	18.9
$\Delta\sigma_{ys}$ calculated from microstructure (MPa)		–	15	43
$\Delta\sigma_{ys}$ measured by pillar compression (MPa)		–	-129 ± 321	-217 ± 264

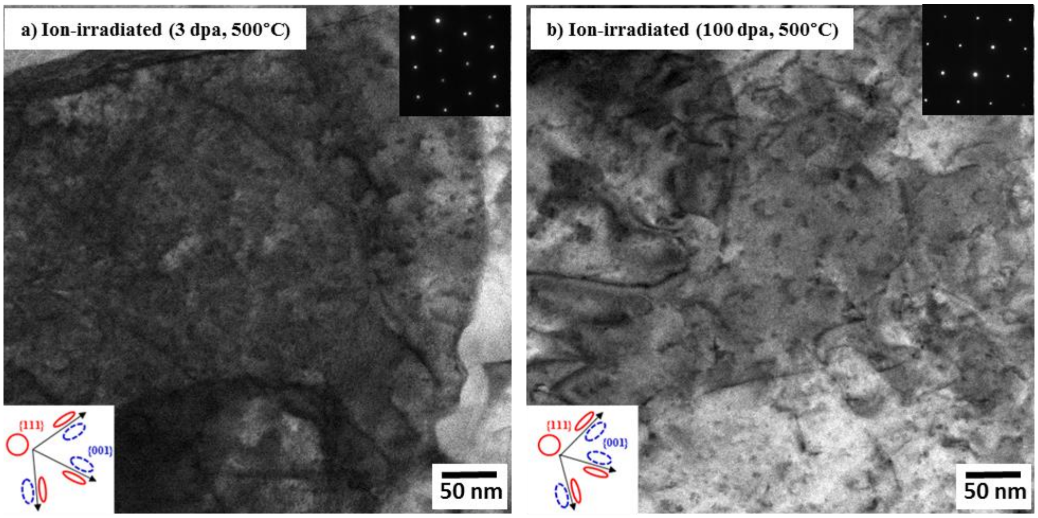

Figure 3.11 Representative dislocation loops in Fe-9%Cr ODS imaged along the [111] zone axis following Fe2+ ion irradiation at 500°C to (a) 3 dpa and (b) 100 dpa

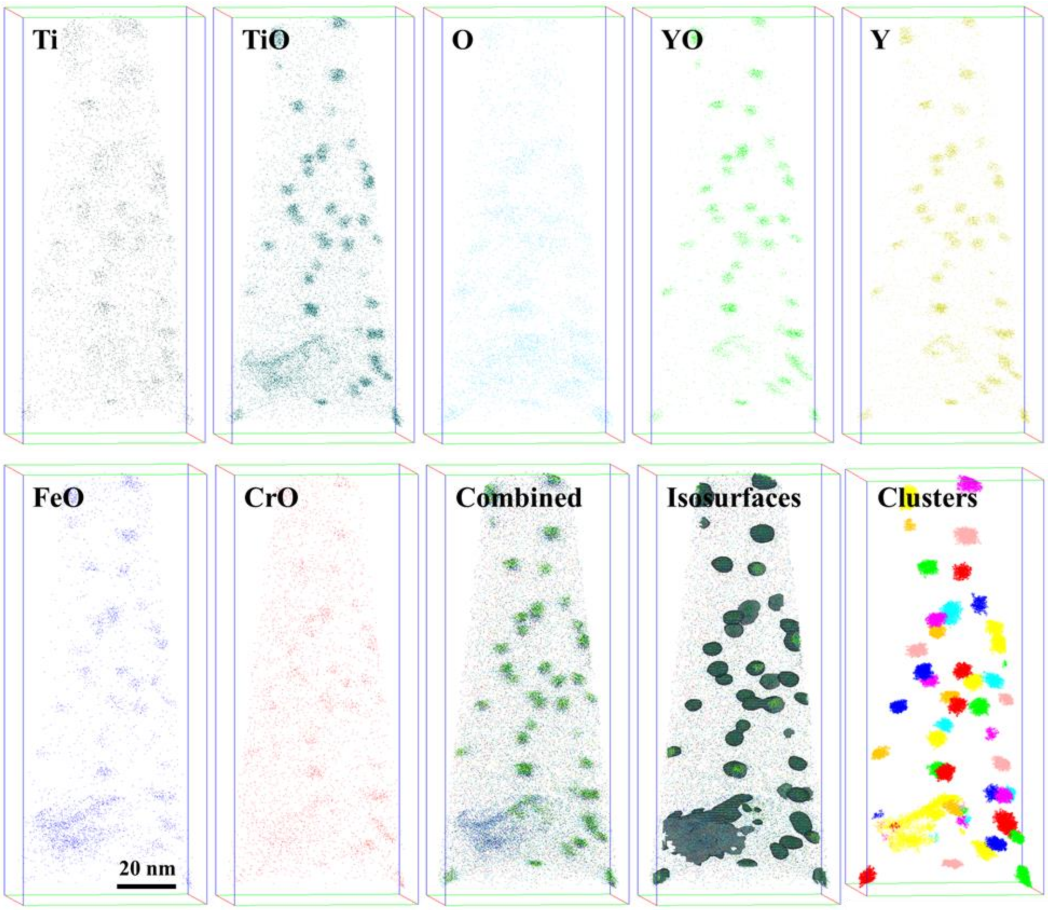

Figure 3.12 Atom probe distribution maps showing oxide nanoclusters in Fe-9%Cr ODS after Fe^{2+} ion irradiation to 3 dpa at 500°C

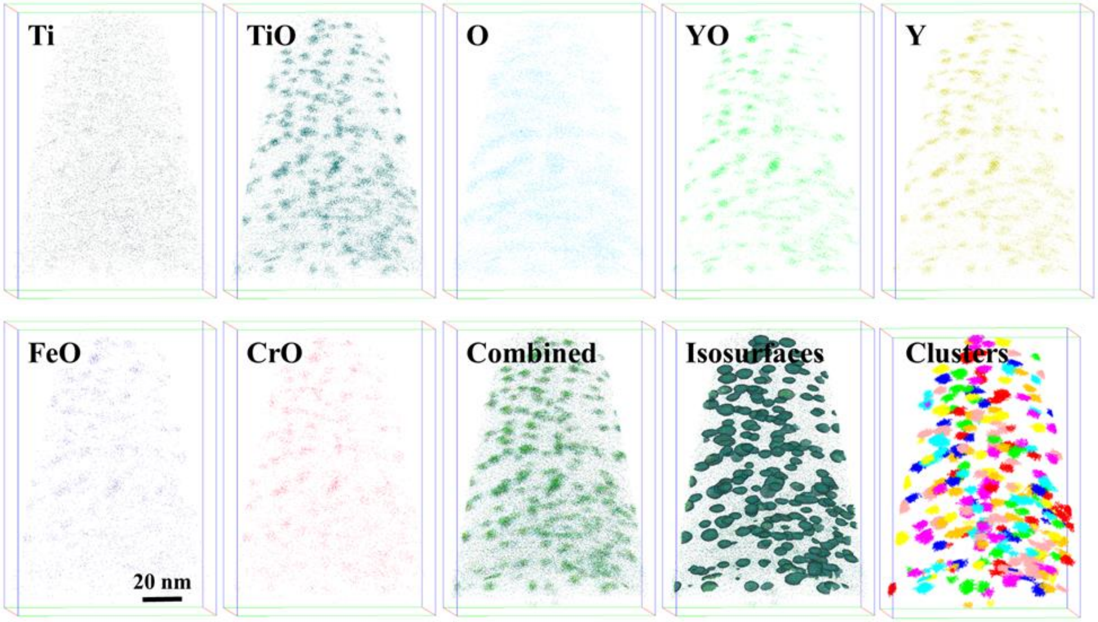

Figure 3.13 Atom probe distribution maps showing oxide nanoclusters in Fe-9%Cr ODS after Fe2+ ion irradiation to 100 dpa at 500°C

3.4 Discussion

3.4.1 Yield Strength

It has been suggested [41] that there is a threshold pillar diameter above which yield strength measured by TEM *in situ* methods is independent of size. This threshold is lower for irradiated materials than for unirradiated materials due to the high density of irradiation-induced obstacles [41]. Since the study herein uses a square or rectangular pillar cross-section, the minimum pillar dimension will be used in place of diameter. By plotting the yield strength as a function of the minimum pillar dimension (Figure 3.9b), the size effect is apparent. In both irradiated conditions, thinner pillars (i.e. those having minimum dimension ≤100 nm) exhibit a wide spread in yield strength (Figure 3.9b, Table 3.2). Although some of these pillars fall within the expected range (highlighted bands, Figure 3.9b), some of these pillars also result in excessively high yield strength measurements. Larger pillars (i.e. those having minimum dimension >100 nm) produce a narrower distribution of yield strengths closer to expected values. These results suggest a potential size effect for irradiated materials similar to that observed by Kiener [41]: measured yield strength plateaus to bulk values with an increasing pillar minimum dimension above >100 nm.

For each specimen condition, the average spacing between obstacles (L_{ob}) on the glide plane is calculated from the microstructure measurements in Table 3.4 using [48]:

$$L_{ob} = \frac{1}{\sqrt{N_{ob}\overline{d_{ob}}}}$$ **Equation 3.4**

in which N_{ob} is the sum number density of all obstacles (oxide clusters and dislocation loops) and $\overline{d_{ob}}$ is the weighted average diameter of the obstacles. Calculated obstacle spacing (Table 3.4) ranges between 17.2 and 33.7 nm and is influenced primarily by the high density of oxide nanoclusters. These values are well below the minimum dimension of each pillar sample studied herein, so it follows that the obstacles – not the pillar dimensions – will be the limiting factor in determining the dislocation source size, which is consistent with references [39,41]. However, as the minimum dimension of pillars approach 100 nm and below (closer to the average obstacle spacing), the influence of the pillar size on the dislocation source size becomes more relevant, leading to a likely size effect for smaller pillars (i.e. < 100 nm). A plausible explanation for why the as-received material exhibits no size effect is that its L_{ob} is smaller than the irradiated steels.

3.4.2 Elastic Modulus

The size effect observed below 100 nm for yield strength can also be seen in the elastic modulus results (Figure 3.10b). The modulus is shown as a function of minimum dimension; pillars with minimum dimension <100 nm have moduli 10-30 GPa lower than those measured from pillars having minimum dimension >100 nm. In addition, regardless of the minimum pillar dimension, the elastic modulus measured by TEM *in situ* compression is approximately an order of magnitude lower than expected values. This discrepancy is attributed to two primary reasons: (1) the deformation is not contained only within in the pillar, but also extends into the base, and (2) the elastic modulus is significantly affected by the inhomogeneity of the microstructure. Both of these factors can be accounted for in our analysis.

Besides removing the visible deflection of the base (as mentioned in the Results section), to account for deformation occurring in both the pillar and the base, we adjust for plasticity occurring below the pillar (i.e. in the base material). First, as mentioned in the results, we subtract the maximum deflection of the base, which is visible in the real-time video of the compression tests, from the maximum displacement measured by the flat punch during the compression test. This is a basic and necessary step to analyzing any of the data. To show the difference, we have quantified the change in the results. The measured elastic modulus increases by a factor of 0.4, to 9.4 GPa (Figure 3.14, “Deflection adjusted”).

However, the modulus generally remains below expected values, especially for the irradiated conditions. The second step, then, is to account for plastic deformation occurring in the base using a FEM. This step follows the approach taken by Imrich [32], which used finite element modeling to reconcile experimental moduli with bulk values for copper. For the work presented herein, a two-dimensional FEM is constructed in ANSYS® Workbench, Academic Research release 15.0 [90], with the pillar and base supported solely along the bottom surface, restricted in the ‘Z-direction’, and using a quadrilateral mesh. Representative FEM simulations are shown in Figure 3.15 (Figure

3.15a for the as received pillar on a 1 μm base, and Figure 3.15b for the 3 dpa pillar on a 5 μm base). According to FEM calculations, the pillar base height has a strong influence on the percent of the displacement occurring in the base relative to in the pillar (Table 3.5).

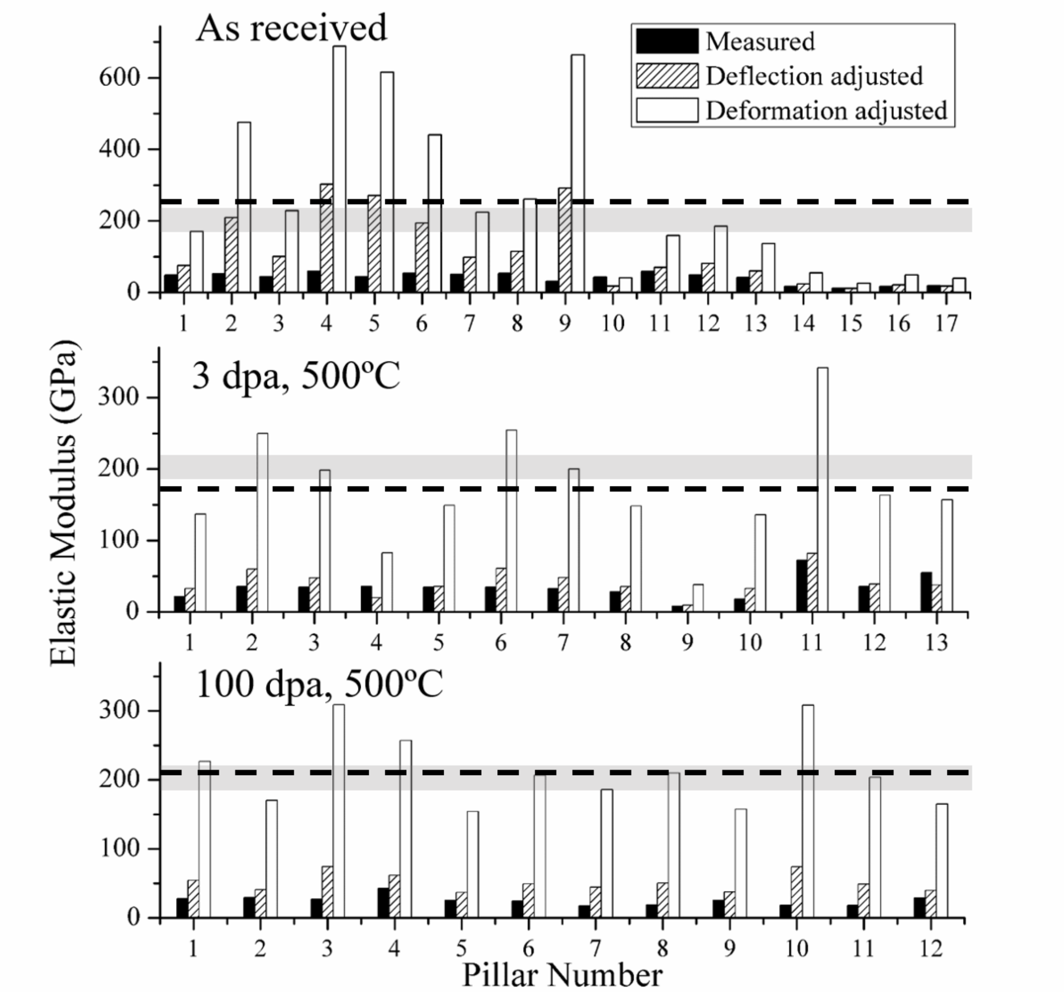

Figure 3.14 Measured and adjusted elastic modulus values for all pillars. Gray shaded band shows expected range (190-220 GPa). Dotted line shows average of the deformation adjusted values in a given condition

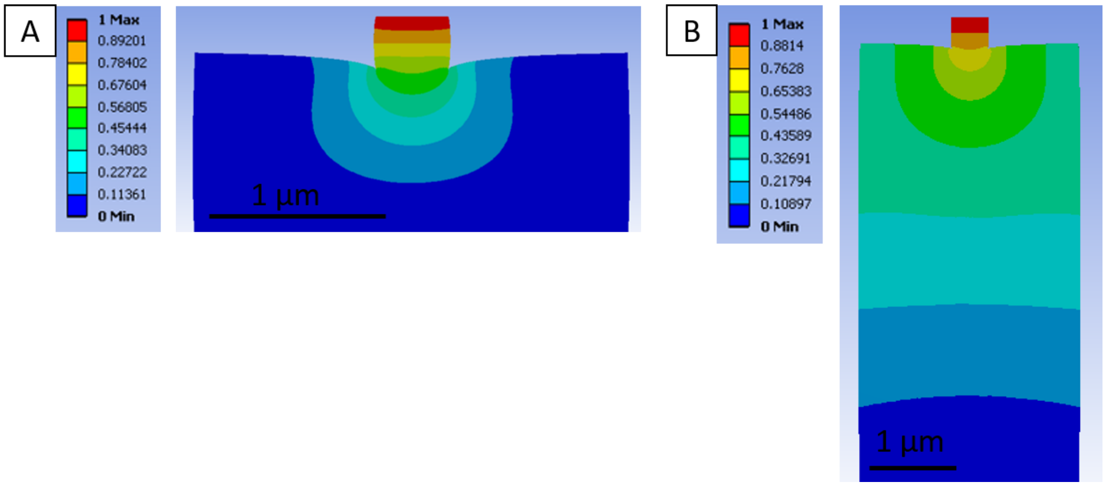

Figure 3.15 FEM showing normalized displacement of (A) as received pillar with 1 µm base and (B) 3 dpa pillar with 5 µm base

Table 3.5 FEM results of percent deformation occurring in pillar and base for varying base heights

Base height (µm)	% deformation in pillar	% deformation in base
1	43	57
3	30	70
5	24	76
6	21	79

For the irradiated conditions, a base height of 5 µm is representative of our pillar fabrication technique, and at this height, 76% of the deformation occurs in the base (and thus only 24% of the deformation occurs in the pillar). Normalizing the measured displacement by this fraction, the irradiated elastic modulus values now fall into closer agreement with bulk values and range from 130 GPa to 309 GPa (Figure 3.14, “Deformation adjusted”). For the as received ODS pillars, some of the deflection adjusted modulus values fall within the expected range (190-220 GPa), even before deformation adjustments are applied. It then follows that the deformation adjusted modulus values exceed the expected range (Figure 3.14). The average difference between deflection adjusted and measured moduli is ~3 times greater for the as received material than for the irradiated conditions, suggesting that the base of the as received material deforms more than the base of the irradiated material.

Even after adjusting irradiated elastic moduli to account for deformation in the base, modulus values span a wide range (130-309 GPa). Microstructural inhomogeneities could explain these variations, especially for the <100 nm pillars. Since the average grain diameter of this material is ~300 nm, only ~14% of a single grain could be contained within a pillar of dimensions of 400 nm × 400 nm × 100 nm. Considering the directionality of elastic modulus, the crystal orientation relative to the compressive direction then becomes a significant factor influencing the measured elastic modulus. For b.c.c. (body centered cubic) iron, elastic modulus calculations can range from 131 GPa in the [100] orientation, to 284 GPa in the [111] direction and have been confirmed experimentally [49,91]. This directionality provides a large enough variation in moduli to explain the range measured in the irradiated moduli (Figure 3.14).

3.4.3 Microstructure Analysis

Irradiation alters the yield strength of the material by changing the size and number density of microstructural obstacles to dislocation motion. This change in yield stress can be predicted from the microstructure using the dispersed barrier model [48]:

$$\Delta\sigma_{ys,i} \propto \sqrt{Nd} \qquad \textbf{Equation 3.5}$$

where $\Delta\sigma_{ys,i}$ represents the contribution to strengthening of microstructural feature i, N is the number density of feature i, and d is the average diameter of feature i. The strengthening contribution of all features are then combined through the root-sum-square approach (Eq, 6), which has been shown to be more accurate than a linear sum approach for this ODS alloy [22]

$$\Delta\sigma_{ys} = \sqrt{\sum_i \left(\Delta\sigma_{ys,i}\right)^2} \qquad \textbf{Equation 3.6}$$

Using the methodology and barrier strength factors (α values) outlined in ref. [22]to estimate the relative strength of each barrier type (dislocation loops and oxide nanoclusters), the predicted total change in yield stress from the microstructure is 15 MPa and 43 MPa (Table 3.4) for specimens ion irradiated to 3 dpa and 100 dpa, respectively. Again, this magnitude of strengthening after 100 dpa is approximately half that observed by Dolph, et al. [65] on the same alloy irradiated to 100 dpa at 400°C, which is reasonable given the higher irradiation temperature (500°C) in this work.

This microstructure-based prediction is consistent, within experimental uncertainties, with the changes in yield strength measured by TEM *in situ* pillar compression: -129 ± 321 MPa and -217 ± 264 MPa for the Fe^{2+} irradiated ODS at 3 dpa and 100 dpa at 500°C, respectively. These results suggest that in the irradiated specimens, strengthening added by the irradiation-induced nucleation of dislocation loops is offset by the softening attributed to the decrease in size and number density of oxide nanoclusters.

3.5 Conclusions

This research demonstrates that TEM *in situ* micropillar compression tests hold great promise for quantitatively determining mechanical properties of small volumes of ion-irradiated materials. We present a versatile method for preparing micropillars from an irradiated bulk specimen, and analyze the compression test results and irradiated microstructures. We conclude:

- Yield strengths measured directly from TEM *in situ* compression pillar tests fall within expected values for the as received and ion irradiated ODS. The high obstacle density, rather than the specimen size, governs dislocation motion.
- Elastic modulus measured directly from TEM *in situ* compression pillar tests are approximately an order of magnitude lower than expected values for the as received and ion irradiated ODS. However, when adjusted for the amount of deformation and deflection in the base material, elastic modulus values fall within the expected range.
- Due to the high density of oxide nanoclusters and the resultant inter-obstacle spacing in the as received and irradiated Fe-9%Cr ODS alloy, a sample size effect is only observed in samples with minimum dimension $\leq$ 100 nm.
- Minimal changes in yield strength following Fe^{2+} irradiation to both 3 dpa and 100 dpa at 500°C are consistent with observed changes in the irradiated microstructures. Strengthening from irradiation-induced dislocation loops is likely offset by the softening due to partial dissolution of oxide nanoclusters.

3.6 Contributions

The work for this article began as a joint effort between fellow graduate student, Matthew Swenson and I. Matthew used it as an independent study credit and at the beginning it was a good way for me to learn the FIB and TEM techniques. However, as results began to come in, the work began to become my own.

The first half of the lab work was conducted by myself and Mr. Swenson. The second half by myself. Mr. Swenson taught me how to use the FIB and helped develop the FIB milling process for the pillars and together we developed the PI95 Picoindenter process. Dr. Yaqiao Wu operated the PI95 Picoindenter within the TEM. However, the mechanical testing parameters were defined by myself.

I collected the load-displacement data and converted it to stress-strain for each of the pillars. The yield strength, elastic modulus, and finite element analysis was all my own work. Mr. Swenson had previously characterized the microstructure of the Fe-9%Cr and his results were published here.

I was the primary author of the article, writing all sections except for 3.3.2 and 3.4.3, which were provided by Matthew Swenson. The paper was edited by Dr. Wharry and Mr. Swenson. The review process was carried out between the Journal of Nuclear Materials and myself.

CHAPTER FOUR: CONCLUSIONS

Due to the unique constraints in testing ion irradiated material, i.e. the shallow damage layer, the *in situ* TEM micropillar compression technique lends itself well to quantifying the mechanical properties of the ion irradiated material. In this study a versatile FIB milling process has been developed for ion irradiated materials. Yield strength and elastic modulus have been found for a model Fe-9%Cr ODS alloy in both the as received and Fe^{2+} irradiated conditions.

Yet, concerns due to size-effects in such small specimens needs to be more fully understood prior to utilizing this technique widely in the field. In this study, *in situ* TEM micropillar compression has been shown to be valid for the ion-irradiated structural and cladding candidate material Fe-9%Cr ODS. The major conclusions of this work are:

1) A size effect is seen in Fe-9%Cr for both the as received and irradiated conditions under micropillar compression.

2) The relationship between the minimum dimension and the obstacle spacing in the glide plane can be identified for any material.

3) For the model Fe-9%Cr ODS alloy used in this study, a minimum dimension of 100 nm and an obstacle spacing of ≈20-30 nm exists.

The relationship between minimum dimension and obstacle spacing can be seen in Figure 4.1. The literature values for irradiated copper [41] and a Ni-based ODS alloy [39] are compared with the results for the model Fe-9%Cr ODS used here.

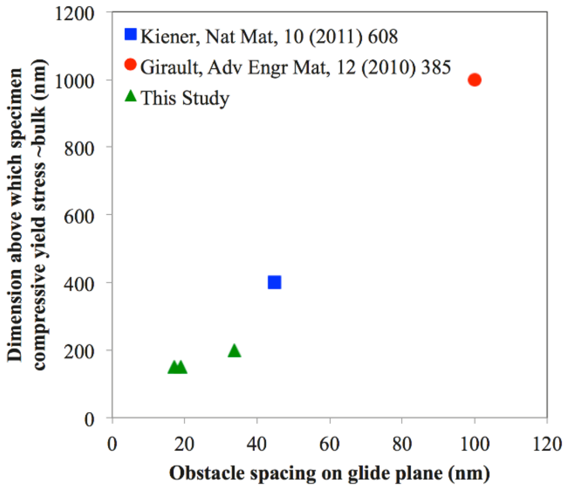

Figure 4.1 **Relationship between obstacle spacing and minimum dimension required for bulk compressive yield stress values demonstrating literature and values found in this work**

As further work is conducted on other alloys using the *in situ* TEM micropillar compression technique, Figure 4.1 will continue to be populated, such that a possible new Hall-Petch-like relationship can be built relating the minimum dimension and obstacle spacing with yield stress in a material.

REFERENCES

[1] S.J. Zinkle, J.T. Busby, Structural materials for fission & fusion energy, Mater. Today. 12 (2009) 12–19. doi:10.1016/S1369-7021(09)70294-9.

[2] T. Allen, J. Busby, M. Meyer, D. Petti, Materials challenges for nuclear systems, Mater. Today. 13 (2010) 14–23. doi:10.1016/S1369-7021(10)70220-0.

[3] K.L. Murty, I. Charit, Structural materials for Gen-IV nuclear reactors: Challenges and opportunities, J. Nucl. Mater. 383 (2008) 189–195. doi:10.1016/j.jnucmat.2008.08.044.

[4] P. Yvon, F. Carré, Structural materials challenges for advanced reactor systems, J. Nucl. Mater. 385 (2009) 217–222. doi:10.1016/j.jnucmat.2008.11.026.

[5] R.L. Klueh, A.T. Nelson, Ferritic/martensitic steels for next-generation reactors, J. Nucl. Mater. 371 (2007) 37–52. doi:10.1016/j.jnucmat.2007.05.005.

[6] D.K. Mukhopadhyay, F.H. Froes, D.S. Gelles, Development of oxide dispersion strengthened ferritic steels for fusion, J. Nucl. Mater. 258–263 (1998) 1209–1215. doi:10.1016/S0022-3115(98)00188-3.

[7] A. Hishinuma, A. Kohyama, R.. Klueh, D.. Gelles, W. Dietz, K. Ehrlich, Current status and future R&D for reduced-activation ferritic/martensitic steels, J. Nucl. Mater. 258–263 (1998) 193–204. doi:10.1016/S0022-3115(98)00395-X.

[8] A. Uehira, S. Ukai, T. Mizuno, Tensile Properties of 11Cr-0.5 Mo-2W, V, Nb Stainless Steel in LMFBR Environment, J. Nucl. Sci. Tech. 3131 (2000) 37–41. doi:10.1080/18811248.2000.9714956.

[9] M. Klimiankou, R. Lindau, A. Möslang, HRTEM study of yttrium oxide particles in ODS steels for fusion reactor application, J. Cryst. Growth. 249 (2003) 381–387. doi:10.1016/S0022-0248(02)02134-6.

[10] R. Lindau, A. Möslang, M. Schirra, P. Schlossmacher, M. Klimenkov, Mechanical and microstructural properties of a hipped RAFM ODS-steel, J. Nucl. Mater. 307–311 (2002) 769–772. doi:10.1016/S0022-3115(02)01045-0.

[11] Y. de Carlan, J.L. Bechade, P. Dubuisson, J.L. Seran, P. Billot, A. Bougault, et al., CEA developments of new ferritic ODS alloys for nuclear applications, J. Nucl. Mater. 386–388 (2009) 430–432. doi:10.1016/j.jnucmat.2008.12.156.

[12] P. Dubuisson, Y. De Carlan, V. Garat, M. Blat, ODS Ferritic/martensitic alloys for Sodium Fast Reactor fuel pin cladding, J. Nucl. Mater. 428 (2012) 6–12. doi:10.1016/j.jnucmat.2011.10.037.

[13] P. Pareige, M.K. Miller, R.E. Stoller, D.T. Hoelzer, E. Cadel, B. Radiguet, Stability of nanometer-sized oxide clusters in mechanically-alloyed steel under ion-induced displacement cascade damage conditions, J. Nucl. Mater. 360 (2007) 136–142. doi:10.1016/j.jnucmat.2006.09.011.

[14] T.R. Allen, J. Gan, J.I. Cole, M.K. Miller, J.T. Busby, S. Shutthanandan, et al., Radiation response of a 9 chromium oxide dispersion strengthened steel to heavy ion irradiation, J. Nucl. Mater. 375 (2008) 26–37. doi:10.1016/j.jnucmat.2007.11.001.

[15] A.G. Certain, K.G. Field, T.R. Allen, M.K. Miller, J. Bentley, J.T. Busby, Response of nanoclusters in a 9Cr ODS steel to 1 dpa, 525˚C proton irradiation, J. Nucl. Mater. 407 (2010) 2–9. doi:10.1016/j.jnucmat.2010.07.002.

[16] A. Certain, S. Kuchibhatla, V. Shutthanandan, D.T. Hoelzer, T.R. Allen, Radiation stability of nanoclusters in nano-structured oxide dispersion strengthened (ODS) steels, J. Nucl. Mater. 434 (2013) 311–321. doi:10.1016/j.jnucmat.2012.11.021.

[17] I. Monnet, P. Dubuisson, Y. Serruys, M.O. Ruault, O. Kaïtasov, B. Jouffrey, Microstructural investigation of the stability under irradiation of oxide dispersion strengthened ferritic steels, J. Nucl. Mater. 335 (2004) 311–321. doi:10.1016/j.jnucmat.2004.05.018.

[18] C. Liu, C. Yu, N. Hashimoto, S. Ohnuki, M. Ando, K. Shiba, et al., Micro-structure and micro-hardness of ODS steels after ion irradiation, J. Nucl. Mater. 417 (2011) 270–273. doi:10.1016/j.jnucmat.2011.01.067.

[19] S. Ukai, M. Fujiwara, Perspective of ODS alloys application in nuclear environments, J. Nucl. Mater. 307–311 (2002) 749–757. doi:10.1016/S0022-3115(02)01043-7.

[20] N. Akasaka, S. Yamashita, T. Yoshitake, S. Ukai, a Kimura, Microstructural changes of neutron irradiated ODS ferritic and martensitic steels, J. Nucl. Mater. 329–333 (2004) 1053–1056. doi:10.1016/j.jnucmat.2004.04.133.

[21] A. Kimura, R. Kasada, A. Kohyama, H. Tanigawa, T. Hirose, K. Shiba, et al., Recent progress in US-Japan collaborative research on ferritic steels R&D, J. Nucl. Mater. 367–370 A (2007) 60–67. doi:10.1016/j.jnucmat.2007.03.013.

[22] M.J. Swenson, C.K. Dolph, J.P. Wharry, The effects of oxide evolution on mechanical properties in irradiated Fe-9%Cr ODS, J. Nucl. Mater. Submitt. Manuscr. 479 (2016) 426–435. doi:10.1016/j.jnucmat.2016.07.022.

[23] M.J. Swenson, J.P. Wharry, The comparison of microstructure and nanocluster evolution in proton and neutron irradiated Fe-9%Cr ODS steel to 3 dpa at 500c, J. Nucl. Mater. 467 (2015) 97–112. doi:10.1016/j.jnucmat.2015.09.022.

[24] H. Tanigawa, M. Ando, Y. Katoh, T. Hirose, H. Sakasegawa, S. Jitsukawa, et al., Response of reduced activation ferritic steels to high-fluence ion-irradiation, J. Nucl. Mater. 297 (2001) 279–284. doi:10.1016/S0022-3115(01)00633-X.

[25] M.A. Pouchon, J. Chen, R. Ghisleni, J. Michler, W. Hoffelner, Characterization of irradiation damage of ferritic ODS alloys with advanced micro-sample methods, Exp. Mech. 50 (2010) 79–84. doi:10.1007/s11340-008-9214-5.

[26] Z. Jiao, J.T. Busby, G.S. Was, Deformation microstructure of proton-irradiated stainless steels, J. Nucl. Mater. 361 (2007) 218–227. doi:10.1016/j.jnucmat.2006.12.012.

[27] B.H. Sencer, G.S. Was, M. Sagisaka, Y. Isobe, G.M. Bond, F.A. Garner, Proton irradiation emulation of PWR neutron damage microstructures in solution

annealed 304 and cold-worked 316 stainless steels, J. Nucl. Mater. 323 (2003) 18–28. doi:10.1016/j.jnucmat.2003.07.007.

[28] G.S. Was, J.T. Busby, T. Allen, E.A. Kenik, A. Jensson, S.M. Bruemmer, et al., Emulation of neutron irradiation effects with protons: Validation of principle, J. Nucl. Mater. 300 (2002) 198–216. doi:10.1016/S0022-3115(01)00751-6.

[29] G.S. Was, Z. Jiao, E. Getto, K. Sun, A.M. Monterrosa, S.A. Maloy, et al., Emulation of reactor irradiation damage using ion beams, Scr. Mater. 88 (2014) 33–36. doi:10.1016/j.scriptamat.2014.06.003.

[30] J. Gan, G.S. Was, Microstructure evolution in austenitic Fe-Cr-Ni alloys irradiated with rotons: Comparison with neutron-irradiated microstructures, J. Nucl. Mater. 297 (2001) 161–175. doi:10.1016/S0022-3115(01)00615-8.

[31] J.F. Ziegler, SRIM, (2013).

[32] P.J. Imrich, C. Kirchlechner, D. Kiener, G. Dehm, In Situ TEM Microcompression of Single and Bicrystalline Samples: Insights and Limitations, JOM. 67 (2015). doi:10.1007/s11837-015-1440-6.

[33] D. Kiener, A.M. Minor, Source truncation and exhaustion: Insights from quantitative in situ TEM tensile testing, Nano Lett. 11 (2011) 3816–3820. doi:10.1021/nl201890s.

[34] D. Kiener, P.J. Guruprasad, S.M. Keralavarma, G. Dehm, a. a. Benzerga, Work hardening in micropillar compression: In situ experiments and modeling, Acta Mater. 59 (2011) 3825–3840. doi:10.1016/j.actamat.2011.03.003.

[35] M.D. Uchic, D.M. Dimiduk, J.N. Florando, W.D. Nix, Sample dimensions influence strength and crystal plasticity., Science. 305 (2004) 986–989. doi:10.1126/science.1098993.

[36] Z. Shan, In situ TEM investigation of the mechanical behavior of micronanoscaled metal pillars, Jom. 64 (2012) 1229–1234. doi:10.1007/s11837-012-0436-8.

[37] R. Fritz, V. Maier-Kiener, D. Lutz, D. Kiener, Interplay between sample size and grain size: Single crystalline vs. ultrafine-grained chromium micropillars, Mater. Sci. Eng. A. 674 (2016) 626–633. doi:10.1016/j.msea.2016.08.015.

[38] J. Ye, R.K. Mishra, A.K. Sachdev, A.M. Minor, In situ TEM compression testing of Mg and Mg-0.2 wt.% Ce single crystals, Scr. Mater. 64 (2011) 292–295. doi:10.1016/j.scriptamat.2010.09.047.

[39] B. Girault, A.S. Schneider, C.P. Prick, E. Arzt, Strength effects in micropillars of a dispersion strengthened superalloy, Adv. Eng. Mater. 12 (2010) 385–388. doi:10.1002/adem.201000089.

[40] D.E.J. Armstrong, C.D. Hardie, J.S.K.L. Gibson, A.J. Bushby, P.D. Edmondson, S.G. Roberts, Small-scale characterisation of irradiated nuclear materials: Part II nanoindentation and micro-cantilever testing of ion irradiated nuclear materials, J. Nucl. Mater. 462 (2015) 374–381. doi:10.1016/j.jnucmat.2015.01.053.

[41] D. Kiener, P. Hosemann, S.A. Maloy, A.M. Minor, In situ nanocompression testing of irradiated copper., Nat. Mater. 10 (2011) 608–613. doi:10.1038/nmat3055.

[42] P. Hosemann, C. Shin, D. Kiener, Small scale mechanical testing of irradiated materials, J. Mater. Res. (2015) 1–15. doi:10.1557/jmr.2015.26.

[43] C. Shin, S. Lim, H. Jin, P. Hosemann, J. Kwon, Development and testing of microcompression for post irradiation characterization of ODS steels, J. Nucl. Mater. 444 (2014) 43–48. doi:10.1016/j.jnucmat.2013.09.025.

[44] W.D.J. Callister, D.G. Rethswich, Materials Science and Engineering, 9th ed., John Wiley & Sons, Inc., Hoboken, New Jersey, 2014.

[45] E. Arzt, Size Effects in Materials Due to Microstructural and Dimensional Constraints: A Comparative Review, Acta Mater. 46 (1998) 5611–5626. doi:10.1177/0261927X99018004006.

[46] T. Tanno, S. Ohtsuka, Y. Yano, T. Kaito, Y. Oba, M. Ohnuma, et al., Evaluation of mechanical properties and nano-meso structures of 9–11%Cr ODS steels, J. Nucl. Mater. 440 (2013) 568–574. doi:10.1016/j.jnucmat.2013.04.006.

[47] S. Ohtsuka, S. Ukai, M. Fujiwara, T. Kaito, T. Narita, Improvement of Creep Strength of 9CrODS Martensitic Steel by Controlling Excess Oxygen and Titanium Concentrations, Mater. Trans. 46 (2005) 487–492.

[48] G.S. Was, Fundamentals of Radiation Materials Science, Springer, New York, 2007.

[49] M. Meyers, K. Chawla, Mechanical Behavior of Materials, Cambridge University Press, New York, 2009.

[50] R.L. Klueh, D.R. Harries, High-Chromium Ferritic and Martensitic Steels for Nuclear Applications, 2001. doi:10.1520/MONO3-EB.

[51] C.K. Dolph, M.J. Swenson, J.P. Wharry, Plastic zone size for nanoindenation of irradiated Fe-9%Cr ODS, (2016).

[52] M.J. Alinger, G.R. Odette, D.T. Hoelzer, The development and stability of Y-Ti-O nanoclusters in mechanically alloyed Fe-Cr based ferritic alloys, J. Nucl. Mater. 329–333 (2004) 382–386. doi:10.1016/j.jnucmat.2004.04.042.

[53] L. Barnard, G.R. Odette, I. Szlufarska, D. Morgan, An ab initio study of Ti-Y-O nanocluster energetics in nanostructured ferritic alloys, Acta Mater. 60 (2012) 935–947. doi:10.1016/j.actamat.2011.11.011.

[54] M.J. Swenson, C.K. Dolph, J.P. Wharry, The effects of oxide evolution on mechanical properties in irradiated Fe-9%Cr ODS, J. Nucl. Mater. (n.d.).

[55] M. Nagini, R. Vijay, M. Ramakrishna, a. V. Reddy, G. Sundararajan, Influence of the duration of high energy ball milling on the microstructure and mechanical properties of a 9Cr oxide dispersion strengthened ferritic–martensitic steel, Mater. Sci. Eng. A. 620 (2015) 490–499. doi:10.1016/j.msea.2014.10.050.

[56] R. Miyata, S. Ukai, X. Wu, N. Oono, S. Hayashi, S. Ohtsuka, et al., Strength correlation with residual ferrite fraction in 9CrODS ferritic steel, J. Nucl. Mater. 442 (2013) 138–141. doi:10.1016/j.jnucmat.2013.04.086.

[57] Z. Shi, F. Han, The microstructure and mechanical properties of micro-scale Y2O3 strengthened 9Cr steel fabricated by vacuum casting, Mater. Des. 66 (2015) 304–308. doi:10.1016/j.matdes.2014.10.075.

[58] B. Fournier, A. Steckmeyer, A.L. Rouffie, J. Malaplate, J. Garnier, M. Ratti, et al., Mechanical behaviour of ferritic ODS steels-Temperature dependancy and anisotropy, J. Nucl. Mater. 430 (2012) 142–149. doi:10.1016/j.jnucmat.2012.05.048.

[59] L. Toualbi, C. Cayron, P. Olier, R. Logé, Y. de Carlan, Relationships between mechanical behavior and microstructural evolutions in Fe 9Cr–ODS during the fabrication route of SFR cladding tubes, J. Nucl. Mater. 442 (2013) 410–416. doi:10.1016/j.jnucmat.2013.04.052.

[60] S. Zinkle, Thermophysical and Mechanical Properties of Fe-(8-9)% Cr reduced activation steels, US. Dept. Energy. Off. Adm. Serv. (1998). http://cds.cern.ch/record/474544.

[61] J. Henry, X. Averty, A. Alamo, Tensile and impact properties of 9Cr tempered martensitic steels and ODS-FeCr alloys irradiated in a fast reactor at 325 ??c up to 78 dpa, J. Nucl. Mater. 417 (2011) 99–103. doi:10.1016/j.jnucmat.2010.12.203.

[62] E. Lucon, A. Leenaers, W. Vandermeulen, Mechanical response of oxide dispersion strengthened (ODS) EUROFER97 after neutron irradiation at 300 ??C, Fusion Eng. Des. 82 (2007) 2438–2443. doi:10.1016/j.fusengdes.2007.05.018.

[63] C.D. Hardie, S.G. Roberts, A.J. Bushby, Understanding the effects of ion irradiation using nanoindentation techniques, J. Nucl. Mater. 462 (2014) 391–401. doi:10.1016/j.jnucmat.2014.11.066.

[64] T. Miura, K. Fujii, K. Fukuya, K. Takashima, Influence of crystal orientation on hardness and nanoindentation deformation in ion-irradiated stainless steels, J. Nucl. Mater. 417 (2011) 984–987. doi:10.1016/j.jnucmat.2010.12.197.

[65] C.K. Dolph, Plastic deformation and effective strain hardening coefficient of irradiated Fe-9wt%Cr ODS alloy by nano-indentation and TEM, Boise State University, 2015.

[66] H. Vo, A. Reichardt, C. Howard, M.D. Abad, D. Kaoumi, P. Chou, et al., Small-Scale Mechanical Testing on Proton Beam-Irradiated 304 SS from Room Temperature to Reactor Operation Temperature, JOM. 67 (2015) 2959–2964. doi:10.1007/s11837-015-1596-0.

[67] J.S. Weaver, S. Pathak, A. Reichardt, H. Vo, S.A. Maloy, P. Hosemann, et al., Spherical nanoindentation of proton irradiation 304 stainless steel: a comparison of small scale mechanical test techniques for measuring irradiation hardening, Rev. (2017).

[68] P. Hosemann, C. Vieh, R.R. Greco, S. Kabra, J.A. Valdez, M.J. Cappiello, et al., Nanoindentation on ion irradiated steels, J. Nucl. Mater. 389 (2009) 239–247. doi:10.1016/j.jnucmat.2009.02.026.

[69] M. Legros, In situ mechanical TEM: Seeing and measuring under stress with electrons, Comptes Rendus Phys. 15 (2014) 224–240. doi:10.1016/j.crhy.2014.02.002.

[70] S. Manchuraju, a. Kroeger, C. Somsen, a. Dlouhy, G. Eggeler, P.M. Sarosi, et al., Pseudoelastic deformation and size effects during in situ transmission electron microscopy tensile testing of NiTi, Acta Mater. 60 (2012) 2770–2777. doi:10.1016/j.actamat.2012.01.043.

[71] D. Kiener, P. Kaufmann, A.M. Minor, Strength, hardening, and failure observed by in situ TEM tensile testing, Adv. Eng. Mater. 14 (2012) 960–967. doi:10.1002/adem.201200031.

[72] D. Zhang, J.-M. Breguet, R. Clavel, L. Phillippe, I. Utke, J. Michler, In situ tensile testing of individual Co nanowires inside a scanning electron microscope., Nanotechnology. 20 (2009) 365706. doi:10.1088/0957-4484/20/36/365706.

[73] F. Mompiou, M. Legros, C. Ensslen, O. Kraft, In situ TEM study of twin boundary migration in sub-micron Be fibers, Acta Mater. 96 (2015) 57–65. doi:10.1016/j.actamat.2015.06.016.

[74] E. A. Withey, A. M. Minor, D.C. Chrzan, J.W. Morris, S. Kuramoto, The deformation of Gum Metal through in situ compression of nanopillars, Acta Mater. 58 (2010) 2652–2665. doi:10.1016/j.actamat.2009.12.052.

[75] D. Kiener, A.M. Minor, O. Anderoglu, Y. Wang, S.A. Maloy, P. Hosemann, Application of small-scale testing for investigation of ion-beam-irradiated materials, J. Mater. Res. 27 (2012) 2724–2736. doi:10.1557/jmr.2012.303.

[76] D. Kiener, C. Motz, G. Dehm, Micro-compression testing: A critical discussion of experimental constraints, Mater. Sci. Eng. A. 505 (2009) 79–87. doi:10.1016/j.msea.2009.01.005.

[77] P.J. Imrich, C. Kirchlechner, D. Kiener, G. Dehm, Internal and external stresses: In situ TEM compression of Cu bicrystals containing a twin boundary, Scr. Mater. 100 (2015) 94–97. doi:10.1016/j.scriptamat.2014.12.023.

[78] C. Heintze, F. Bergner, M. Hernández-Mayoral, Ion-irradiation-induced damage in Fe-Cr alloys characterized by nanoindentation, J. Nucl. Mater. 417 (2011) 980–983. doi:10.1016/j.jnucmat.2010.12.196.

[79] N. Li, E.G. Fu, H. Wang, J.J. Carter, L. Shao, S.A. Maloy, et al., He ion irradiation damage in Fe/W nanolayer films, J. Nucl. Mater. 389 (2009) 233–238. doi:10.1016/j.jnucmat.2009.02.007.

[80] P. Hosemann, J.G. Swadener, D. Kiener, G.S. Was, S.A. Maloy, N. Li, An exploratory study to determine applicability of nano-hardness and micro-compression measurements for yield stress estimation, J. Nucl. Mater. 375 (2008) 135–143. doi:10.1016/j.jnucmat.2007.11.004.

[81] L.A. Giannuzzi, J.L. Drown, S.R. Brown, R.B. Irwin, F.A. Stevie, Applications of the FIB lift-out technique for TEM specimen preparation, Microsc. Res. Tech. 41 (1998) 285–290. doi:10.1002/(SICI)1097-0029(19980515)41:4<285::AID-JEMT1>3.0.CO;2-Q.

[82] D. Kiener, C. Motz, T. Schöberl, M. Jenko, G. Dehm, Determination of Mechanical Properties of Copper at the Micron Scale, Adv. Eng. Mater. 8 (2006) 1119–1125. doi:10.1002/adem.200600129.

[83] C.M. Parish, K.G. Field, A.G. Certain, J.P. Wharry, Application of STEM characterization for investigating radiation effects in BCC Fe-based alloys, J. Mater. Res. 30 (2015) 1275–1289. doi:10.1557/jmr.2015.32.

[84] B. Yao, D.J. Edwards, R.J. Kurtz, TEM characterization of dislocation loops in irradiated bcc Fe-based steels, J. Nucl. Mater. 434 (2013) 402–410. doi:10.1016/j.jnucmat.2012.12.002.

[85] J.M. Hyde, E.A. Marquis, K.B. Wilford, T.J. Williams, A sensitivity analysis of the maximum separation method for the characterisation of solute clusters, Ultramicroscopy. 111 (2011) 440–447. doi:10.1016/j.ultramic.2010.12.015.

[86] R.P. Kolli, D.N. Seidman, Comparison of compositional and morphological atom-probe tomography analyses for a multicomponent Fe-Cu steel, Microsc. Microanal. 13 (2007) 272–84. doi:10.1017/S1431927607070675.

[87] C.A. Williams, D. Haley, E.A. Marquis, G.D.W. Smith, M.P. Moody, Defining clusters in APT reconstructions of ODS steels, Ultramicroscopy. 132 (2013) 271–278. doi:10.1016/j.ultramic.2012.12.011.

[88] M.K. Miller, R. Forbes, Atom Probe Tomography: The Local Electrode Atom Probe, Springer, New York, 2014.

[89] C.A. Williams, E.A. Marquis, A. Cerezo, G.D.W. Smith, Nanoscale characterisation of ODS-Eurofer 97 steel: An atom-probe tomography study, J. Nucl. Mater. 400 (2010) 37–45. doi:10.1016/j.jnucmat.2010.02.007.

[90] A. Inc., ANSYS Workbench, Academic Research, (n.d.).

[91] G. Zhang, Z. Zhou, K. Mo, Y. Miao, S. Li, X. Liu, et al., The comparison of microstructures and mechanical properties between 14Cr-Al and 14Cr-Ti ferritic ODS alloys, Mater. Des. 98 (2016) 61–67. doi:10.1016/j.matdes.2016.02.117.

APPENDIX A

In Situ TEM Micropillar Compression Video Recording

Please see the online ScholarWorks archive for the electronic copy of an *in situ* TEM micropillar compression test conducted on Fe-9%Cr ODS. The pillar geometry is 400 nm × 400 nm × 100 nm and the material is in the as received condition.